Biomaterials 287 (2022) 121663

Contents lists available at ScienceDirect

Biomaterials

journal homepage: www.elsevier.com/locate/biomaterials

# High-strength biodegradable zinc alloy implants with antibacterial and osteogenic properties for the treatment of MRSA-induced rat osteomyelitis

Bo Jia [a,c,1], Zechuan Zhang [b,1], Yifu Zhuang [d,1], Hongtao Yang [e], Yu Han [a], Qiang Wu [a], Xiufeng Jia [f], Yanhui Yin [g], Xinhua Qu [c], Yufeng Zheng [b,**], Kerong Dai [a,*]

[a] Department of Orthopaedic Surgery, Shanghai Key Laboratory of Orthopaedic Implants, Shanghai Ninth People's Hospital, Shanghai Jiaotong University, School of Medicine, Shanghai, 200011, China
[b] School of Materials Science and Engineering, Peking University, Beijing, 100871, China
[c] Department of Bone and Joint Surgery, Renji Hospital, School of Medicine, Shanghai Jiao Tong University, Shanghai, 200127, China
[d] Trauma Center, Department of Orthopaedics and Traumatology, Shanghai General Hospital, Shanghai Jiaotong University, Shanghai, 201620, China
[e] School of Engineering Medicine, Beihang University, Beijing, 100191, China
[f] Department of Orthopaedic Surgery, Wudi People's Hospital, Binzhou, 251900, China
[g] School of Economics and Trade, Shandong Management University, Jinan, 250357, China

ARTICLE INFO

*Keywords:*
Biodegradable metals
Zn-Li-Ag alloy
Antibacterial
Implant-related infections
Osteogenesis

ABSTRACT

Implant-related infections caused by drug-resistant bacteria remain a major challenge faced by orthopedic surgeons. Furthermore, ideal prevention and treatment methods are lacking in clinical practice. Here, based on the antibacterial and osteogenic properties of Zn alloys, Ag and Li were selected as alloying elements to prepare biodegradable Zn-Li-Ag ternary alloys. Li and Ag addition improved the mechanical properties of Zn-Li-Ag alloys. The Zn-0.8Li-0.5Ag alloy exhibited the highest ultimate tensile strength (>530 MPa). Zn-Li-Ag alloys showed strong bactericidal effects on methicillin-resistant *Staphylococcus aureus* (MRSA) *in vitro*. RNA sequencing revealed two MRSA-killing mechanisms exhibited by the Zn-0.8Li-0.5Ag alloy: cellular metabolism disturbance and induction of reactive oxygen species production. To verify that the therapeutic potential of the Zn-0.8Li-0.5Ag alloy is greater than that of Ti intramedullary nails, X-ray, micro-computed tomography, microbiological, and histological analyses were conducted in a rat femoral model of MRSA-induced osteomyelitis. Treatment with Zn-0.8Li-0.5Ag alloy implants resulted in remarkable infection control and favorable bone retention. The *in vivo* safety of this ternary alloy was confirmed by evaluating vital organ functions and pathological morphologies. We suggest that, with its good antibacterial and osteogenic properties, Zn-0.8Li-0.5Ag alloy can serve as an orthopedic implant material to prevent and treat orthopedic implant-related infections.

## 1. Introduction

Osteomyelitis is an inflammatory reaction to microbial infections accompanied by progressive bone loss [1]. The dominant causative pathogenic bacteria of osteomyelitis are staphylococci, including *Staphylococcus aureus* and *Staphylococcus epidermidis* [2]. According to its etiology, osteomyelitis can be classified into three types. One type is caused by local bacterial colonization and is mainly found in post-traumatic wounds and following various orthopedic surgeries; this type is closely related to the use of implants. The second type is caused by insufficient blood supply, which is often secondary to soft tissue infection in the feet of patients with diabetes. The last type is hematogenic, which is most common in children [1]. The incidence of osteomyelitis can be very high in susceptible patients. In patients with open trauma, the incidence of osteomyelitis can reach 20% [3]. In patients with a diabetic foot, approximately 12–20% of cases can progress to infections of the surrounding bone tissues [4]; in severe cases, the incidence of osteomyelitis can reach 66% [5]. Once osteomyelitis occurs, osteogenic activities are inhibited and osteoclastic functions are activated, which can cause osteoporosis and pathological fractures [6].

* Corresponding author. Department of Orthopaedics, Ninth People's Hospital, Shanghai Jiao Tong University, School of Medicine, 639 Zhizaoju Road, Shanghai, 200011, China.
** Corresponding author.
*E-mail addresses:* yfzheng@pku.edu.cn (Y. Zheng), krdai@163.com (K. Dai).
[1] These authors contributed equally to this study.

https://doi.org/10.1016/j.biomaterials.2022.121663
Received 3 July 2021; Received in revised form 25 June 2022; Accepted 28 June 2022
Available online 5 July 2022

Additionally, treating osteomyelitis often requires a second operation for thorough debridement, which often exacerbates bone loss. Despite great progress in osteomyelitis treatment, approximately 40% of patients suffer from relapses or long-term infections [2], which makes osteomyelitis one of the most challenging problems in clinical orthopedics.

At present, prevention and treatment methods for osteomyelitis mainly include thorough debridement, the application of sufficient antibiotics for an adequate course of treatment (intravenous or oral; for no less than 4–6 weeks), dead space treatment after debridement (bone substitution materials), and the local application of antibacterial materials. Among them, thorough debridement is the premise, and the application of sufficient antibiotics for an adequate treatment course is the key to eradicating residual bacteria. However, the destruction of blood supply at the infection site leads to local bone tissue necrosis, making it difficult for antibiotics and inflammatory cells to reach this avascular area. Therefore, a sufficient disinfectant concentration cannot be reached in this local area, leading to a poor disinfection effect [1]. However, after an infection occurs, bacteria adhere to each other and accumulate to form a biofilm. The biofilm acts as a protective barrier for bacteria and hinders the penetration of antibiotics, which can inhibit the bactericidal efficiency of antibiotics [7]. Furthermore, the emergence and widespread prevalence of drug-resistant bacteria, represented by methicillin-resistant *S. aureus* (MRSA), have further affected the efficacy of antibiotics. According to the World Health Organization and Centers for Disease Control and Prevention, drug-resistant bacterial infections cause more than 23,000 deaths in the European Union and the United States each year [8], among which, MRSA is the leading cause of mortality [9]. In orthopedics, 60% of implant-related infections are caused by *S. aureus* [10], especially MRSA, which are difficult to treat and can notably prolong the length and cost of hospitalization, cause failure of internal fixation, and lead to disability or even death [11]. Therefore, the emergence of drug-resistant bacteria has presented new challenges to the prevention and treatment of orthopedic infections.

The application of implants is another major risk factor for the occurrence of osteomyelitis. Implant-related infections are the top priority for preventing and treating osteomyelitis [12]. When implants are implanted into the body, they cause local foreign body inflammation, reduce the local immune response, and lead to locus immunodeficiency [13], thereby making it easier for bacteria to colonize and induce infection. The implant surface can also provide suitable conditions for bacterial adhesion and biofilm formation, thereby making it more likely for infections to occur [14]. Therefore, the risk of infection is higher in the presence of implants. A study has shown that osteomyelitis can be induced by significantly fewer *S. aureus* in the presence of implants than in cases without implants [15]. The risk of infection increases significantly after implantation and remains as long as implants are in the body. In addition, as the infection may be latent and delayed, a long-term sustained anti-infective approach is crucial.

Given the existing dilemma of osteomyelitis prevention and treatment, biodegradable orthopedic implant materials with sustained antibacterial activity can be expected to address the abovementioned problems. The appearance of biodegradable Zn-based metals has recently attracted the attention of our research group, and a series of studies on their orthopedic applications have been conducted [16–19]. Biodegradable Zn-based metals are known for their bioactive properties, such as biocompatibility and osteogenic activities; they have become a viable new choice of implant materials in orthopedics [20–22]. More importantly, the good antibacterial ability of $Zn^{2+}$ has been widely reported [23–25]. Biodegradable Zn-based metals can corrode to release $Zn^{2+}$ both *in vivo* and *in vitro*, demonstrating their notable antibacterial properties. Unlike antibiotics, when a biodegradable Zn-based metal is locally applied as an implant material, it can effectively ameliorate the problem of poor disinfection effect resulting from insufficient local antibiotic concentrations. However, the bactericidal mechanism of biodegradable Zn-based metals differs from that of antibiotics; thus, these metals can be expected to improve the killing effect on MRSA and other drug-resistant bacteria. Most importantly, as a biodegradable antibacterial implant material, the Zn-based alloy implant exhibits a sustained antibacterial ability. The osteogenic activity of $Zn^{2+}$ can also effectively improve bone destruction and loss caused by an infection. Moreover, after executing its functions as an implant, these implants will gradually degrade and eventually disappear. Therefore, biodegradable Zn-based alloys can be expected to address the high infection risk caused by residual implants, thereby preventing implant-related infections originating from the source.

In a series of preliminary studies, we confirmed the good osteogenic activity of Zn alloys [19,22] and found that Zn-Li alloys have the best mechanical strength [20]. Zn-Li alloys can meet the demand for internal fixation applications in orthopedic load-bearing areas and are used to repair femoral shaft fractures in rabbits. Zn-Cu [17] and Zn-Ag alloys have satisfactory antibacterial activity; however, Zn-Ag alloys are superior. Zn-Ag alloys [26] are effective in killing bacteria associated with orthopedic infections *in vitro*, including *S. aureus*, *S. epidermidis*, and MRSA. Zn-Ag alloys also effectively inhibit osteoclastic activities at the injured bone site and protect against bone loss while preventing and treating an infection. Therefore, in this study, both Ag and Li were selected as alloying elements to prepare the Zn-Li-Ag ternary alloy system. This was ensured while considering the antibacterial activity and mechanical strength of Zn alloys to meet the mechanical requirements of implant applications in orthopedic load-bearing areas. Therefore, in this study, we designed and prepared novel orthopedic implant materials with both mechanical strength and antibacterial activity to provide a novel strategy for the prevention and treatment of osteomyelitis.

## 2. Materials and methods

### 2.1. Preparation of Zn-Li-Ag alloys and extracts

The metal raw materials used in this study were prepared by melting high-purity zinc (99.99%, Alfa Aesar, UK), lithium (99.95%, Alfa Aesar, UK), and silver (99.99%, Alfa Aesar, UK) ingot according to each alloy's composition, as listed in Table 1. In all prepared alloys, the weight percentage of Li was fixed at 0.8% (higher Li content results in a significant decrease in strength [27]). By varying the weight percentage of Ag (0%, 0.5%, 1.0%, 1.25%, 2.0%, and 3.0%), the corresponding alloys were prepared and named Zn-0.8Li, Zn-0.8Li-0.5Ag, Zn-0.8Li-1.0Ag, Zn-0.8Li-1.25Ag, Zn-0.8Li-2.0Ag, and Zn-0.8Li-3.0Ag, respectively. Before extrusion, the metal ingot was fully homogenized at 350 °C for 48 h and quenched in water. The samples were kept at 260 °C for 2 h before extrusion. The extrusion ratio was 16, the extrusion speed was 1 mm/s, and rods with a diameter of 10 mm were extruded. The metal rods were then cut into disks ($\Phi = 10 \times 1$ mm) and cylinders ($\Phi = 1.5 \times 20$ mm), which were mechanically polished to 2000 mesh. The polished samples were then ultrasonically cleaned in ethanol and acetone and dried at room temperature. Before conducting cell and animal experiments, samples were sterilized with ethylene oxide.

The extracts were prepared according to the ISO10993 standard. The Zn-Li and Zn-Li-Ag alloy metal sheets were immersed in α-minimum

**Table 1**
Analyzed compositions of the studied Zn-Li-Ag alloys and control group.

| Nominal Composition (wt.%) | Analyzed Composition (wt.%) | | |
|---|---|---|---|
| | Li | Ag | Zn |
| Zn-0.8Li | 0.79 | N/A | Balance |
| Zn-0.8Li-0.5Ag | 0.86 | 0.54 | Balance |
| Zn-0.8Li-1.0Ag | 0.77 | 1.02 | Balance |
| Zn-0.8Li-1.25Ag | 0.79 | 1.28 | Balance |
| Zn-0.8Li-3.0Ag | 0.79 | 3.05 | Balance |
| Zn-0.8Li-2.0Ag | 0.84 | 1.97 | Balance |
| Zn-1.0Li-2.0Ag | 1.02 | 2.01 | Balance |

essential medium (α-MEM; Gibco; Grand Island, NY, USA) according to the volume/surface area ratio of 1.25 mL/cm$^2$. The sheets were then transferred into an incubator (Tethys Fisher, UK) at 37 °C in an atmosphere of 5% $CO_2$. After 24 h of immersion, extracts were collected and filtered using a 0.25-μm sterile filter. The prepared extracts were stored at 4 °C for use within 3 days.

### 2.2. Material characterization

#### 2.2.1. Zn-Li-Ag alloy microstructure characteristics and mechanical properties tests

The samples were further polished to 7000 mesh, buffed with a 0.1-μm diamond abrasive paste, and washed with deionized water. All samples were then etched in a 4% $HNO_3$/ethanol solution for 5–10 s. An optical metallographic microscope (Olympus BX51 M, Olympus, Tokyo, Japan) was used to observe and analyze the microstructure of samples. An X-ray diffractometer (XRD; Rigaku DMAX 2400; Rigaku, Japan) using CuKα radiation was used to analyze the structures of the materials. The operating voltage was 40 kV, the current was 100 mA, the scanning range was 10–90°, the scanning speed was 2°/min, and the step size was 0.02°.

Samples used for tensile and compression tests were prepared according to the ASTM E8-04 and ASTM E9-89 standards, respectively. The mechanical properties of materials were tested using a universal material testing machine (Instron 5969; Instron, USA) at room temperature. The strain rate of the tensile test was $1 \times 10^{-4}$/s. Yield strength (YS) was defined as the stress that causes 0.2% plastic deformation. A microhardness tester (Shimadzu HMV-2T; Shimadzu, Japan) was used to measure the Vickers hardness of materials (indentation force: 0.1 kN; holding time: 15 s). At least five samples were selected for each test, and the average values were taken.

#### 2.2.2. Electrochemical test

The electrochemical test was conducted at room temperature using an electrochemical workstation (Autolab; Metrohm, Switzerland) in a simulated body fluid (SBF) (NaCl 8.035 g/L, $NaHCO_3$ 0.355 g/L, KCl 0.25 g/L, $K_2HPO_4{\cdot}3H_2O$ 0.231 g/L, $MgCl_2{\cdot}6H_2O$ 0.311 g/L, HCl (36–38%) 39 mL/L, $CaCl_2$ 0.292 g/L, $Na_2SO_4$ 0.072 g/L, Tris 6.118 g/L, pH 7.4) [20]. A three-electrode system of a platinum electrode-saturated calomel electrode (SCE) was selected to perform the electrochemical test. The open-circuit potential (OCP) of each sample was monitored for 5400 s. Under the measured OCP, electrochemical impedance was measured by electrochemical impedance spectroscopy (EIS) at a measurement frequency of $10^5$–$10^{-2}$ Hz. Then, the polarization curves of materials were recorded at a scan rate of 1 mV/s, a scan voltage range of -500 to 500 mV vs. OCP, and a scan area of 0.2826 cm$^2$ ($\Phi = 6$ mm). Finally, the corrosion potential (Ecorr) and corrosion current density (Icorr) were calculated using Tafel extrapolation analysis. Each alloy type was evaluated at least five times, and the average values were taken.

#### 2.2.3. Immersion experiment

The samples were immersed in SBF at 37 °C for 90 d. According to the ASTM G31-72 standard, the ratio of solution volume to the material surface area was controlled at 20 mL/cm$^2$. After immersion, the samples were washed with distilled water and dried at room temperature. The surface corrosion products of materials were cleaned using a solution containing 200 g/L $CrO_3$. The surface corrosion morphologies both before and after the cleaning step were observed using a high-precision image measuring instrument and a scanning electron microscope (SEM; Hitachi S-4800; Hitachi, Japan). The *in vitro* corrosion rate was calculated according to the following formula: $C = k\Delta m/\rho At$, where C is the corrosion rate in μm/year, k is a constant (k = 1000), Δm is the weight change (g), ρ is the material density (g/mm$^3$), A is the initial immersion surface area (mm$^2$), and t is time (year). Each group of samples was evaluated with at least five specimens to obtain the average value.

### 2.3. In vitro evaluation of antibacterial performance

Based on the results of material properties and cell compatibility, the Zn-0.8Li-0.5Ag, Zn-0.8Li-1.25Ag, and Zn-0.8Li-2.0Ag alloys were selected for antibacterial experiments. The antibacterial characteristics of these three ternary alloys were evaluated and compared with two controls, namely, Zn-0.8Li alloy and pure Ti. MRSA (ATCC 43300) was chosen as an experimental bacterium to evaluate the killing effect of biodegradable Zn-Li-Ag alloys on common drug-resistant bacteria in orthopedics. Tryptone soy broth (TSB), prepared by dissolving 3 g of soy peptone, 17 g of tryptone, 2.5 g of potassium dihydrogen phosphate, 5 g of sodium chloride, and 2.5 g of glucose in 1000 mL of distilled water, was used as the bacterial culture medium [28]. MRSA was suspended in TSB and incubated in a shaker (180 rpm, 37 °C) for 16 h. Finally, the MRSA solution was diluted to the predetermined concentrations.

#### 2.3.1. Bacteriostatic ring test

After 100 μL of MRSA suspension ($1 \times 10^7$ colony-forming units [CFU]/mL) was evenly coated on TSA (Tryptone soy agar) plates, the pure Ti, Zn-0.8Li, Zn-0.8Li-0.5Ag, Zn-0.8Li-1.25Ag, and Zn-0.8Li-2.0Ag alloy metal disks were gently placed at the center of the plate. The antibacterial efficiencies of degradation products obtained from biodegradable Zn-Li and Zn-Li-Ag alloys were determined by the diameter of the antibacterial ring through agar diffusion. After incubating for 24 h in a 37 °C incubator, the plates were photographed, and the diameters of zones of inhibition were measured.

#### 2.3.2. Exploration of the bactericidal mechanism of Zn-Li-Ag alloys

After comprehensive consideration of its material properties, cytocompatibility, and antibacterial performance *in vitro*, the Zn-0.8Li-0.5Ag alloy was selected for investigating its mechanism of killing MRSA. The sterilized pure Ti and Zn-0.8Li-0.5Ag alloy metal disks were placed in a 12-well plate with three replicate samples in each group, and 2 mL of bacterial suspension ($1 \times 10^6$ CFU/mL) was added to each well. Bacterial pellets were collected after cocultivation in a 37 °C incubator for 24 h. Subsequently, the total bacterial RNA was extracted, and RNA sequencing was performed (Wuhan Servicebio Co., Ltd., Wuhan, China). The whole genome sequencing workflow (version 7.0.1, Illumina) was used for data analysis. Finally, the differences in bacterial gene expression between Zn-0.8Li-0.5Ag alloy and pure Ti groups were compared using DESeq2 (version 1.16.1, Illumina).

#### 2.3.3. Reactive oxygen species (ROS) production measurement

Based on our bacterial RNA sequencing results and the relevant reports on the bactericidal mechanisms of $Zn^{2+}$ and $Ag^+$ [29,30], we suggest that the induction of catalytic ROS production is one of the main mechanisms by which Zn-Li-Ag alloys exert bactericidal activity. Therefore, MRSA suspensions were cocultured with pure Ti or Zn-Li-Ag alloy metal disks in 12-well plates with three replicates per group, and 2 mL of MRSA suspension ($1 \times 10^6$ CFU/mL) was added to each well. After 12 and 24 h coculture, the ROS production level was detected using the Reactive Oxygen Species Assay Kit (Beyotime, China). The bactericidal mechanism of the Zn-Li-Ag alloy was then verified.

### 2.4. In vivo anti-infective evaluation in an MRSA-induced rat femoral osteomyelitis model

#### 2.4.1. Surgical procedure

The experimental animals used herein were 3-month-old male Sprague–Dawley rats with an average body weight of 300.93 ± 6.09 g. All animal operations and experiments were approved by the Animal Ethics Committee of Shanghai Rat & Mouse Biotech Co., Ltd. The Zn-0.8Li-0.5Ag alloy was prepared into Φ1.5 × 20 mm nails, and pure Ti nails of the same dimensions were used as a control. The experiment was conducted in two parts. The first part aimed to establish a model of femoral osteomyelitis induced by MRSA. The rats were anesthetized by

intraperitoneally injecting ketamine (10 mg/kg) and 2% xylazine, and the skins of their right hindlimbs were prepared for surgery. The knee joint of the rat was fixed in the maximum flexion position, and a 15-mm longitudinal incision was made along the lateral patella under sterile conditions. The dislocated knee joint was separated layer by layer to expose the femoral condyle. A 1-mm drill was then used to drill the center of the femoral condyle in the direction of the medullary cavity. Then, the bone debris was washed with saline, and 100 μL of $1 \times 10^8$ CFU/mL bacterial suspension was injected into the femoral medullary cavity with a 1-mL syringe. Finally, the drill hole was sealed with bone wax, and the incision was closed layer by layer. Buprenorphine (0.3 mg/kg; Temgesic, Reckitt & Colman, Hull, UK) was injected subcutaneously for postoperative analgesia. In total, 45 rats were used to establish the infection model, and 15 additional rats were used as blank controls. Three weeks after the modeling surgery, X-ray examination was performed to assess the modeling effect, and hematoxylin and eosin (H&E) staining and Giemsa staining were used to evaluate the modeling effect of osteomyelitis.

The second part of the surgical procedure was the implantation of the materials to treat the MRSA-induced infection 3 weeks after the modeling surgery. After conventional anesthesia and skin preparation, the femoral condyle was exposed along the original surgical incision. After full debridement and irrigation, a 1.5-mm hole was drilled into the center of the femoral condyle in the direction of the medullary cavity. After saline irrigation, the Zn-0.8Li-0.5Ag alloy or pure Ti intramedullary nails were implanted into the femoral medullary cavity. The surgical site was washed with saline again and the incision was closed layer by layer. Four rats died during surgery; thus, after implantation of the intramedullary nails, each experimental group was as follows: 15 normal rats in the blank control group; 20 rats in the control group with pure Ti intramedullary nails; and 21 rats in the experimental group with Zn-0.8Li-0.5Ag alloy intramedullary nails. At 3 and 6 weeks after the implantation of intramedullary nails, the rats in each group were euthanized and the relevant tissues/organs were harvested for subsequent analyses.

#### 2.4.2. General condition of animals and evaluation of hematological indices

After the operation, the rats were returned to their cages, fed a normal diet, and allowed to move freely. Wound healing progress, body weights, and body temperatures were monitored regularly. Six weeks after the second implantation operation, blood samples were taken from the rat heart for routine blood tests to evaluate the systemic infection status.

#### 2.4.3. X-ray observation

X-ray images of the rat femur were taken 3 weeks after the infection modeling surgery, as well as 3 and 6 weeks after the second implantation operation. The osteomyelitis model was evaluated 3 weeks after the surgery. The treatment effect of the alloys on osteomyelitis induced in rat femurs was evaluated 3 and 6 weeks after the second operation. According to the literature, quantitative X-ray evaluation was performed to detect periosteal elevation, sequestration, architectural deformation, bone shaft widening, and soft tissue deformation. A score of 0–3 was given for each feature. A higher score indicates a more serious infection [31].

#### 2.4.4. Micro-computed tomography (micro-CT)

At 3 and 6 weeks after the second implantation operation, the rats in each group were euthanized to obtain right femurs. After being immersed in paraformaldehyde, rat femur specimens were scanned by micro-CT (Sanco Micro-ct100, Switzerland). The detailed scanning parameters are provided in Table S1. After the scan was completed, the region of interest (ROI) for data analysis was defined as a 3-mm-high cylindrical area of 1 mm outside the circumference of the intramedullary nail in the femoral condyle (excluding the intramedullary nail). The bone mineral densities (BMD), bone volume (BV), bone volume fraction (BV/TV), trabecular numbers (Tb.N), trabecular thickness (Tb.Th), and trabecular separation (Tb.Sp) were analyzed quantitatively to evaluate the femoral bone weight retention of rats in each group.

#### 2.4.5. In vivo microbiological evaluation

Three and six weeks after the second implantation operation, the rats in each group were euthanized to sample their right femurs, and implants in the femoral medullary cavities were removed. At each time point, four random implants were selected from each group to observe the bacterial adhesion and biofilm formation on the implant surface by SEM. Then, another four implants were selected randomly and treated ultrasonically (50 Hz, 10 min, B3500S-MT, China) to collect the bacteria adhering to the implant surface [32]. After diluting the bacterial suspension 20-fold, the bacteria were plated and cultured for 24 h. The number of bacterial CFUs per plate was then counted to evaluate the number of adhering bacteria on the implant surface.

#### 2.4.6. Histomorphological analysis

Three weeks after the infection modeling surgery, soft tissue sections were sampled from rat femurs for H&E and Giemsa staining to further evaluate the modeling effect of osteomyelitis. Three and six weeks after the second implantation operation, rats in each group were euthanized to sample their right femurs, from which the implants were removed. Next, rat femur specimens were fixed in 4% paraformaldehyde, decalcified in 10% EDTA for 6 weeks, and soft tissue section staining was performed. After ethanol gradient dehydration, the tissues were embedded in paraffin and sectioned for H&E and Giemsa staining to evaluate the treatment status of osteomyelitis. Masson staining, toluidine blue staining, and TRAP staining were performed to assess bone destruction. The stained sections were then observed and imaged under a high-resolution microscope (Olympus CKX41; Olympus, Japan).

#### 2.4.7. Immunohistochemistry

Three and six weeks after the second implantation operation, all rats were euthanized to sample their right femurs. After decalcification, embedding, and sectioning, the immunohistochemical technique was used to detect osteomyelitis-related indices in rat femurs, including inflammatory cells (neutrophils, CD68-labeled macrophages), inflammatory factors (interleukin-10 [IL-10] and tumor necrosis factor α [TNF-α]), and MRSA expression. After staining was completed, the sections were scanned and photographed using a panoramic section scanner (PANNORAMIC DESK/MIDI/250/1000, 3DHISTECH, Hungary), and then semi-quantitative analysis of the expression intensity of each index was performed using scanning and viewing software (CaseViewer2.4, 3DHISTECH, Hungary) and analysis software (Halo v3.0.311.314, Indica Labs, USA).

### 2.5. Data analysis

The SPSS 25.0 statistical software (SPSS Inc. Chicago, IL, USA) was used for data analysis. Quantitative data are expressed as mean ± standard deviation (SD). The data were analyzed using an independent sample *t*-test and one-way analysis of variance (ANOVA). The p-value was set at $^*p < 0.05$ or $^{**}p < 0.01$ to indicate statistically significant differences.

## 3. Results

### 3.1. Material surface microstructure and mechanical strength

The metallographic analysis results of the Zn-0.8Li and Zn-0.8Li-xAg alloys are shown in Fig. 1a. The addition of Ag resulted in a significant change in the microstructure of the material. The metallographic structure of Zn-0.8Li was mainly dendritic. With the addition of Ag, the second phases in Zn-Li-xAg alloys exhibited a different morphology.

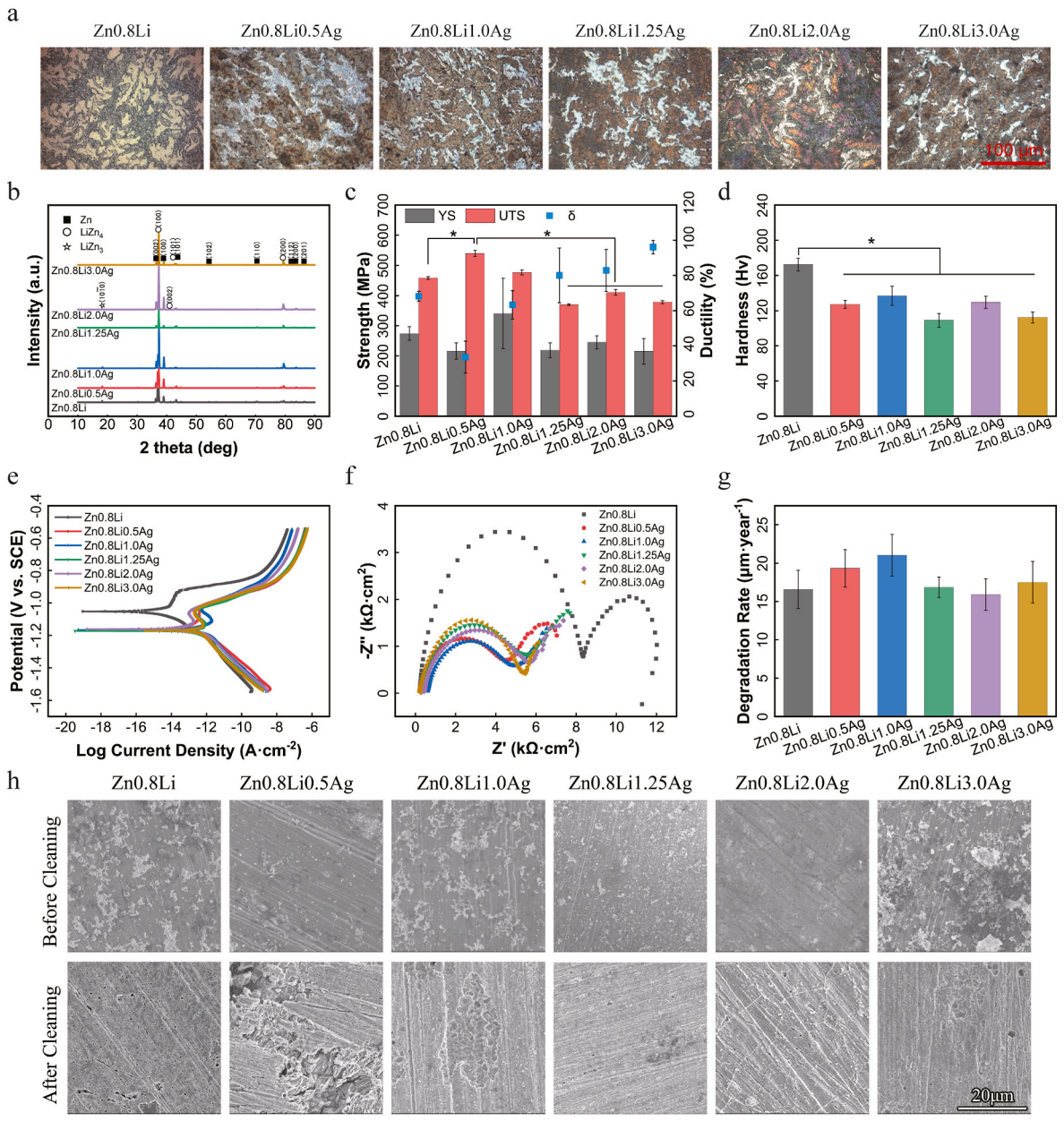


**Fig. 1.** Microstructure, mechanical properties, and *in vitro* corrosion behaviors of Zn-0.8Li-xAg alloys. (a) Microstructure of alloys observed under an optical metallographic microscope at a normal observation direction; (b) X-ray diffraction, (c) yield strength (YS), ultimate tensile strength (UTS), and elongation (δ), (d) Vickers hardness, (e) polarization curves, (f) EIS, and (g) corrosion rates of Zn-Li-Ag alloys; (h) scanning electron microscope (SEM) observation of experimental samples after immersion in simulated body fluid (SBF) solution for 90 d. Data represent the mean ± standard deviation (*$p < 0.05$).

First, the contrast of colors between the matrix phase and second phase was more obvious, showing that the second phases in Zn-Li-xAg alloys had a brighter color than in the Zn-0.8Li alloy. Second, with Ag content increasing, the dendritic structure was decreased in the alloys after extrusion, whereas the river-like structure was increased. Even with a small amount of Ag (0.5 wt%), changes were observed in the metallographic structure. The XRD results in Fig. 1b further show that the second phase comprises Li and Zn, in which the results of $LiZn_4$ are labeled according to the PDF 04-011-9312, and the results of $LiZn_3$ are labeled according to a calculated result [33]. No second phase of Zn and Ag was found. The reason might be that Ag has a high solid solubility in Zn, and the Ag would be in a solid state under a low Ag content [34]. The solid solution of Ag in Zn would change the corrosion potential of the matrix phases, which would further change the potential difference between the matrix phases and second phases. Therefore, during the metallographic analysis, the etching degree of different phases was different in the Zn-0.8Li-xAg alloys. Thus, the dendritic phases of Zn-0.8Li-xAg alloys and Zn-0.8Li showed different colors.

Fig. 1c shows the YS, ultimate tensile strength (UTS), and elongation (Elong) of Zn-0.8Li-xAg alloys. Zn-0.8Li-0.5Ag and Zn-0.8Li-1.0Ag alloys had significantly higher mechanical strengths than the Zn-0.8Li alloy, indicating that there is an optimal range of Ag for improving the strength of the Zn alloy. Moreover, among all designed material compositions, the Zn-0.8Li-0.5Ag alloy had the best UTS, which reached 539.89 ± 10.26 MPa. Fig. 1d shows the Vickers hardness of each alloy group. After the addition of Ag, the Vickers hardness of the alloys was significantly lower than that of the Zn-0.8Li binary alloy.

### 3.2. *In vitro* corrosion behavior

The polarization curve (Fig. 1e) and EIS (Fig. 1f) were used to evaluate the *in vitro* degradation behavior of Zn-0.8Li-xAg alloys. The polarization curves show that the corrosion potential of Zn-0.8Li-xAg alloys was lower than that of the Zn-0.8Li binary alloy. The impedance spectrum curves show that the impedance rings of Zn-0.8Li-xAg were smaller than those of the Zn-0.8Li alloy. The results of both

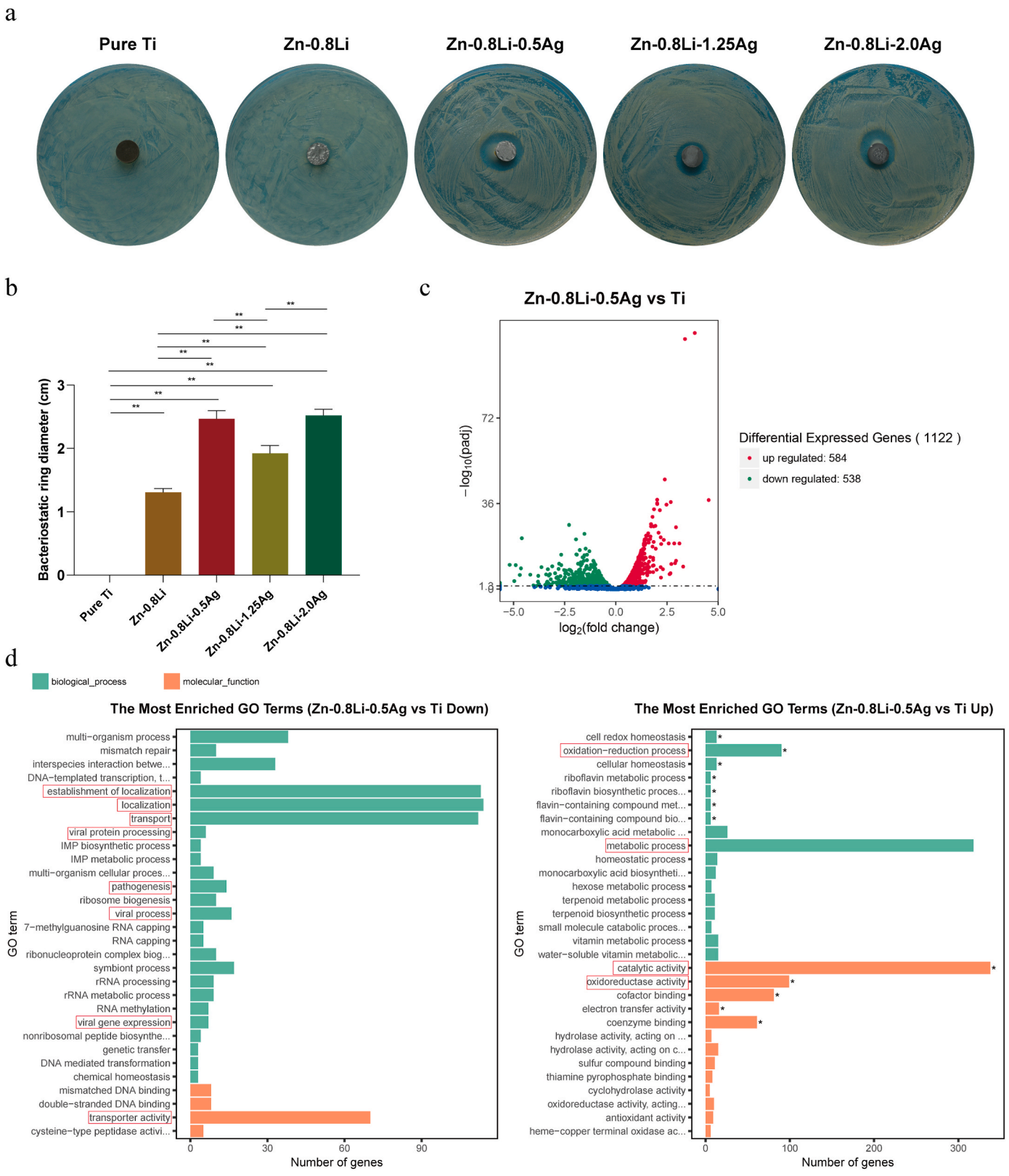


**Fig. 2.** (a) Images and (b) quantitative results of bacteriostatic ring tests. (c) Gene expression differences and (d) main biological functions of the downregulated and upregulated genes in the Zn-0.8Li-0.5Ag alloy group compared with those in the pure Ti group. Data represent the mean ± standard deviation (**$p < 0.01$).

electrochemical tests showed that the Zn-0.8Li-xAg alloys exhibited faster corrosion rates than the Zn-0.8Li alloy. The results of the electrochemical tests also showed that the polarization and impedance spectrum curves of each Zn-0.8Li-xAg alloy were close to each other, indicating similar corrosion behaviors among Zn-0.8Li-xAg alloys. Fig. 1g shows the results of 90 d of corrosion immersion. The addition of Ag did not cause a significant difference in the long-term degradation rate of the Zn-0.8Li alloy.

After being immersed in SBF solution for 90 d, the morphologies of the experimental samples were assessed before and after cleaning the corrosion products. Fig. S1 shows the overall macroscopic morphologies of the samples and Fig. 1h shows the results of SEM. Different corrosion macromorphologies of the alloys show that the Zn-0.8Li and Zn-0.8Li-xAg alloys mainly exhibited uniform corrosion morphology with pitting corrosion, and the Zn-0.8Li-xAg alloys had more numerous and finer corrosion pits. The images of the corrosion micromorphologies obtained by SEM show that both Zn-0.8Li and Zn-0.8Li-xAg alloys had corrosion micropits and microcracks, and the Zn-0.8Li-xAg alloys had more numerous and denser corrosion micropits.

### 3.3. In vitro antibacterial evaluation of Zn-Li-Ag alloys

#### 3.3.1. Bacteriostatic ring test

The bacteriostatic ring results of the Zn-0.8Li-xAg alloys are shown in Fig. 2a and b. The pure Ti sheet had no antibacterial ability, as no bacteriostatic ring formation was observed. The Zn-0.8Li alloy exhibited a certain antibacterial ability. The bacteriostatic rings of the three Zn-0.8Li-xAg alloys were enlarged to varying extents compared with those in the Zn-0.8Li control group, suggesting better antibacterial properties. Among the three alloys, Zn-0.8Li-0.5Ag and Zn-0.8Li-2.0Ag exhibited the best antibacterial abilities.

#### 3.3.2. MRSA-killing mechanism of the Zn-0.8Li-0.5Ag alloy

The difference in gene expression between the Zn-0.8Li-0.5Ag alloy group and the pure Ti group is shown in Fig. 2c. Fig. 2d shows the main biological functions of the downregulated and upregulated genes in the Zn-0.8Li-0.5Ag alloy group compared with those of the pure Ti group. Genes that are essential for the basic biological metabolism of bacteria, including genes related to the establishment of localization, transport, and transporter activity, were significantly inhibited. Genes related to bacterial virulence were also significantly inhibited. Bacteria in the Zn-0.8Li-0.5Ag alloy group had significantly stronger metabolic reactions, catalytic activities, and redox reactions.

Fig. 3a shows the quantitative detection results of related genes. Localization-related and transport-related genes were significantly inhibited. Furthermore, the Zn-0.8Li-0.5Ag alloy could also reduce bacterial virulence, inhibit bacterial biofilm formation, and affect genes related to bacterial drug resistance. The levels of ROS production after coincubation of Zn-0.8Li-0.5Ag alloy metal sheets with MRSA suspension for 12 and 24 h are shown in Fig. 3b. There was a significantly greater amount of ROS production in the bacterial suspension of the Zn-0.8Li-0.5Ag alloy group, which verified that the Zn-0.8Li-0.5Ag alloy can exert catalytic activity to induce ROS production.

Fig. 3c is a diagram illustrating a possible MRSA-killing mechanism of Zn-0.8Li-0.5Ag. It is believed that the Zn-0.8Li-0.5Ag alloy may kill MRSA mainly by affecting their basic biological metabolism and inducing ROS production. In addition to killing bacteria, the alloy affected their virulence, biofilm formation, and drug resistance.

### 3.4. Evaluation of the Zn-0.8Li-0.5Ag alloy treatment effect on MRSA-induced osteomyelitis in vivo

The basic workflow of the animal experiments is illustrated in Fig. 4a.

#### 3.4.1. General conditions and hematological evaluation

The body weight and body temperature results are shown in Fig. 4b. After implanting intramedullary nails at 3 weeks, the slow reduction in body weight and persistent low fever in the pure Ti group rats indicated signs of chronic systemic infection. However, the fact that the rats gradually recovered their body weight and temperature demonstrated responses to improving systemic infection. Table S2 shows the routine blood test results of blood collected from the rat hearts during sampling 6 weeks after the second debridement and intramedullary nail implantation. The white blood cell (WBC) count, percentage of neutrophils (NETU%), and absolute neutrophils (NETU#) in the pure Ti group were all significantly higher than those in the Zn-0.8Li-0.5Ag alloy and blank control groups. Among the three indices, the WBC count and NEUT# in the pure Ti group were significantly higher than those in the Zn-0.8Li-0.5Ag alloy group ($^{**}p < 0.01$). These results confirmed a significantly milder systemic infection response in the Zn-0.8Li-0.5Ag alloy group, indicating the favorable treatment effects of the Zn-0.8Li-0.5Ag alloy in the MRSA-induced osteomyelitis model.

#### 3.4.2. Gross observations and X-ray evaluation results

The gross observations of the specimens of rat femurs are shown in Fig. 4c. After the modeling surgery, the femoral shaft in the MRSA group became significantly thicker than that in the blank group, indicating signs of infection. At 3 and 6 weeks after intramedullary nail implantation, the rat femoral shaft specimens further thickened in the pure Ti group with hyperemia and sinus tract formation, indicating progression of osteomyelitis. Moreover, in the Zn-0.8Li-0.5Ag alloy group, the signs of femoral infection in rats were significantly relieved, and the gross morphology recovered to normal 6 weeks after the operation. This finding indicated that osteomyelitis was controlled.

The X-ray results in different groups of rat femurs at different time points are shown in Fig. 4d. Three weeks after the MRSA bacterial suspension was injected into the rat femoral medullary cavity, cortical bone destruction, osteolysis, periosteal reaction, and double-line signs were observed in rat femurs (red arrows), suggesting chronic osteomyelitis. At 3 weeks after the second implantation operation, the X-ray results showed that the infection signs in the pure Ti group were still obvious, whereas those in the Zn-0.8Li-0.5Ag alloy group were controlled significantly. The X-ray results obtained 6 weeks after the second implantation operation verified this result. The results of the quantitative X-ray evaluation are shown in Fig. 4e. Compared with that in the pure Ti implant group, the significantly decreased infection score confirmed the satisfactory anti-infection ability of the Zn-0.8Li-0.5Ag alloy *in vivo*.

#### 3.4.3. Micro-CT scan results

The micro-CT scan results of rat femurs obtained 3 and 6 weeks after the second implantation operation are shown in Fig. 5, and Fig. 5a shows a two-dimensional micro-CT scan image (coronal sections), a three-dimensional sagittal reconstruction, and a three-dimensional ROI reconstruction (yellow labels highlight the intramedullary nail, white labels indicate the newly formed bone). Signs of femoral infection, such as obvious osteolysis and bone loss, were observed in the pure Ti group. However, in the Zn-0.8Li-0.5Ag alloy group, no bone loss was observed in rat femurs. Instead, a small amount of degradation products and a large amount of newly formed bone could be seen around the intramedullary nail. Fig. 5b shows the quantitative results of BMD, BV, BV/TV, Tb.N, Tb.Th, and Tb.Sp in the ROI. The Zn-0.8Li-0.5Ag alloy group had higher BMD, more newly formed BV, higher Tb.N, and lower Tb.Sp than the pure Ti group. These results verified the better bone retention effect in the Zn-0.8Li-0.5Ag group.

#### 3.4.4. In vivo microbiological evaluation results

The SEM results of the implant surface are shown in Fig. S2a. At 3 and 6 weeks after implantation, the surface of the pure Ti intramedullary nail showed a mound- and lump-shaped adhesion with bacteria wrapped inside, indicating the formation of a bacterial biofilm on the surface of

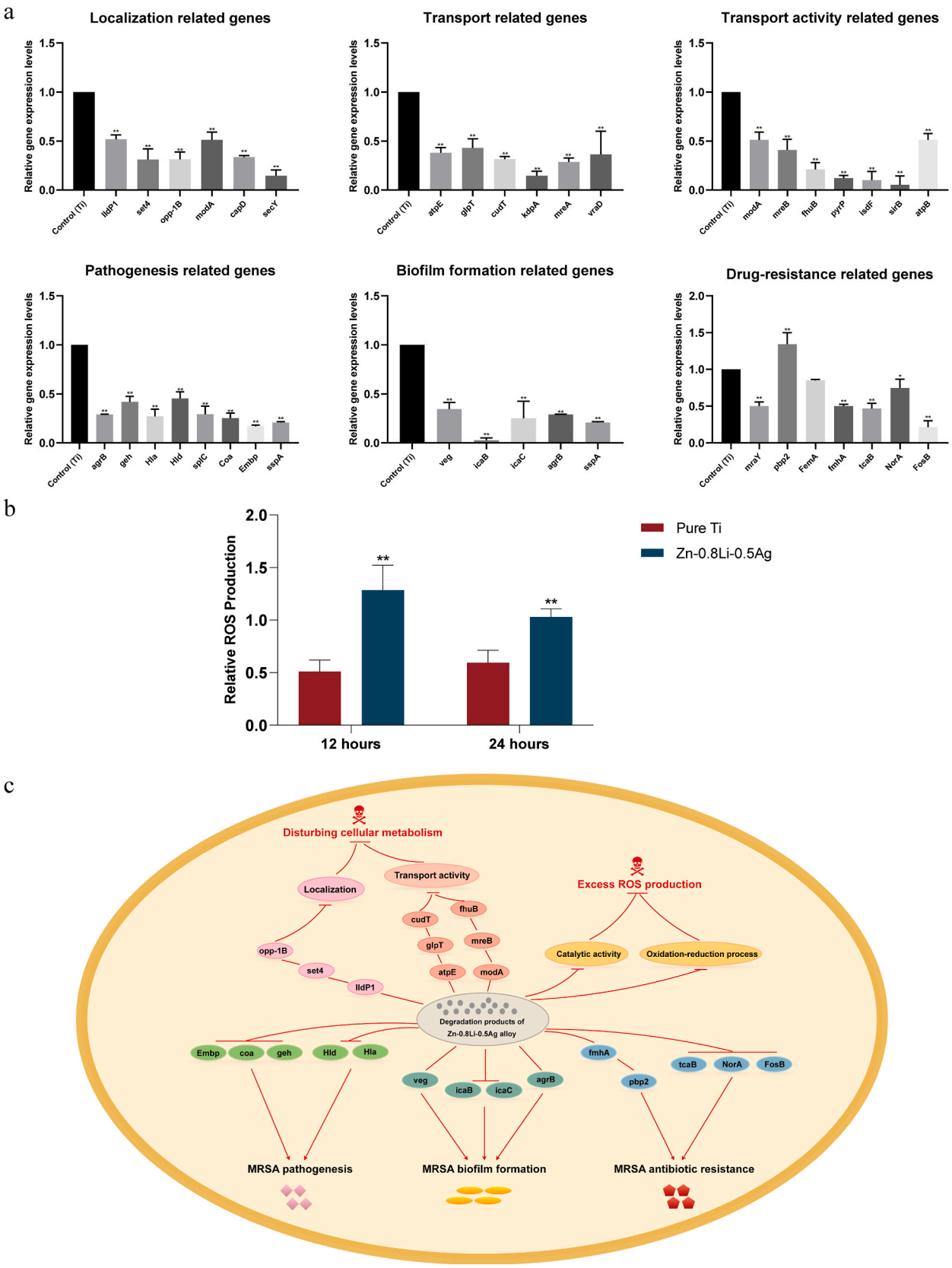


**Fig. 3.** MRSA-killing mechanism of the Zn-0.8Li-0.5Ag alloy. (a) Quantitative results of gene expression related to localization, transport, transport activity, pathogenesis, biofilm formation, and drug resistance of MRSA and (b) reactive oxygen species (ROS) production levels in the Zn-0.8Li-0.5Ag alloy and pure Ti groups after coincubation with MRSA suspension for 12 and 24 h. (c) Suggested mechanism underlying the antimicrobial properties of the Zn-0.8Li-0.5Ag alloy against MRSA. Data represent the mean ± standard deviation (*$p < 0.05$, **$p < 0.01$).

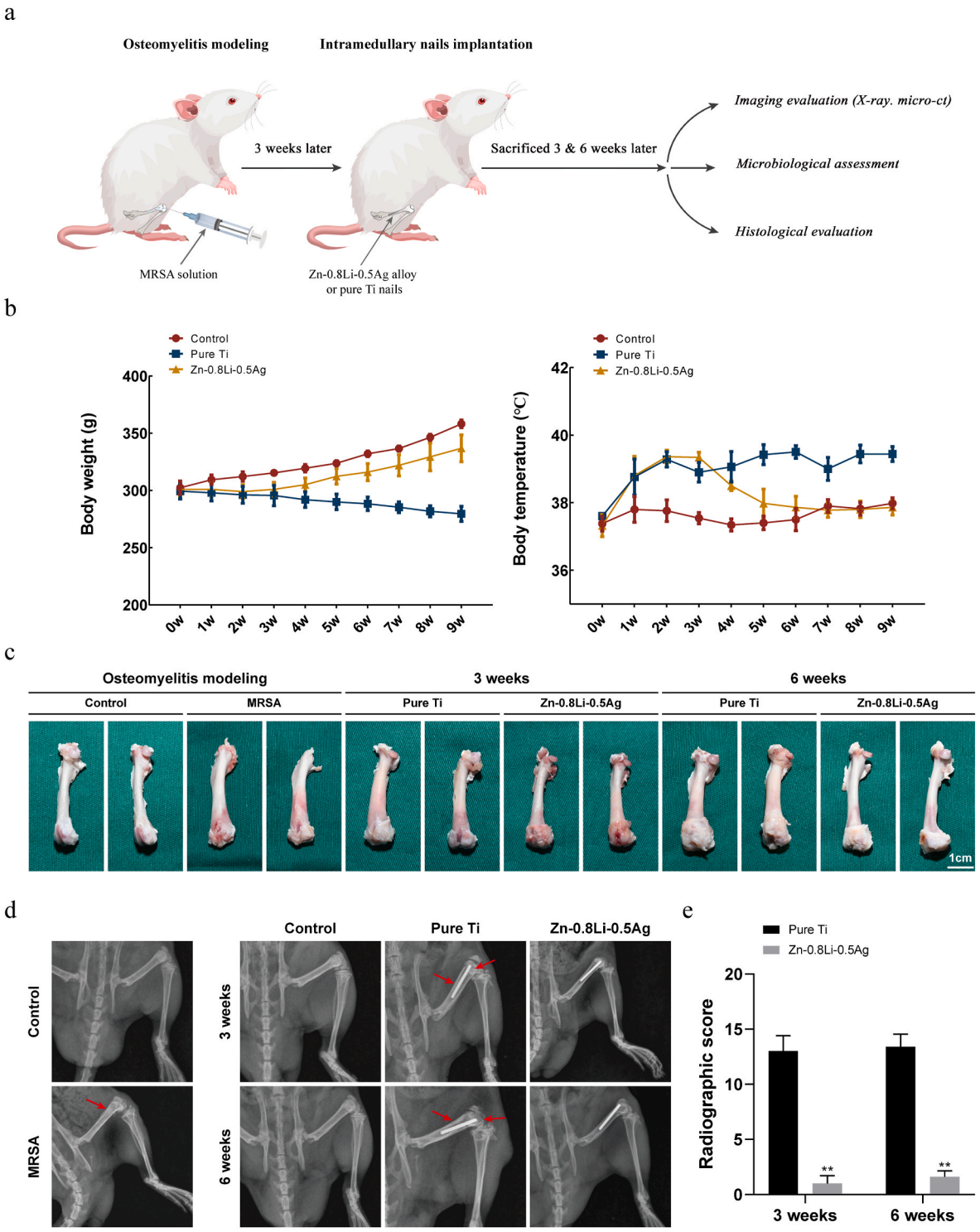


**Fig. 4.** (a) Basic workflow of the animal experiments. (b) Trends of body weight (g) and body temperature (°C) of rats in different groups. (c) Gross observations of rat femurs at indicated times. (d) Digital X-ray images and (e) quantitative results of rat femurs at indicated times. The control group comprised animals with no treatment. Data represent the mean ± standard deviation (**$p < 0.01$).

the pure Ti intramedullary nail. Under high magnification, the bacteria had normal morphologies and were distributed in clusters. On the surface of the Zn-0.8Li-0.5Ag alloy intramedullary nail, bacteria could hardly be seen; it could only be observed that the surface of the Zn-0.8Li-0.5Ag alloy nail had degraded and cracked. This observation demonstrated that bacteria could not adhere and grow on the Zn-0.8Li-0.5Ag alloy surface, thereby demonstrating its good antibacterial properties. After ultrasonically treating the implant surface, the bacterial suspensions were diluted and plated, and bacterial colony growth was evaluated (Fig. S2b and c). There were significantly fewer bacterial CFUs in the Zn-0.8Li-0.5Ag alloy group, which confirmed its satisfactory antibacterial properties.

### 3.4.5. *Histological evaluation results*

The H&E and Giemsa staining results of soft tissue sections are shown in Fig. 6. Fig. 6a and b show the results of H&E staining, and the former

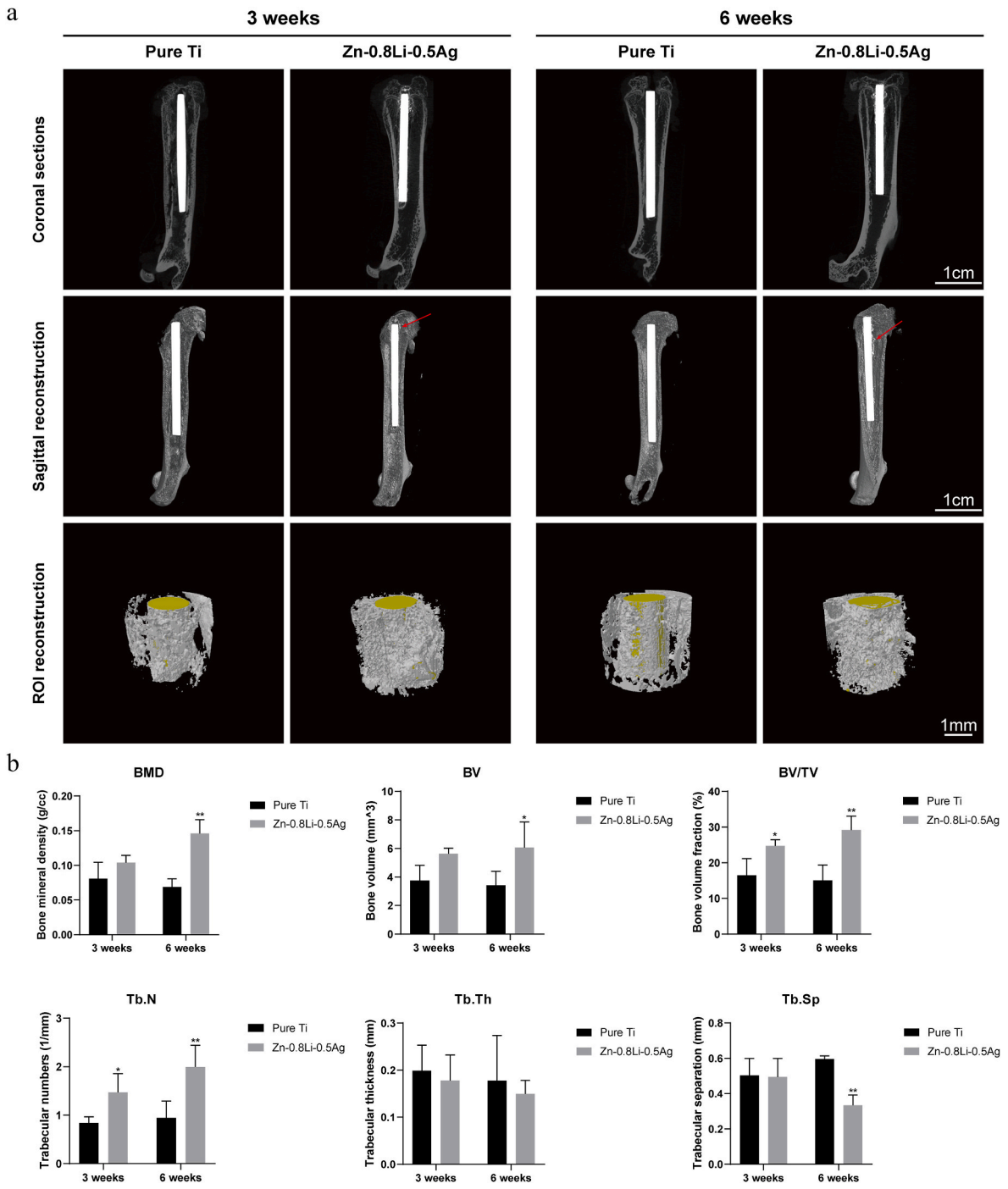


**Fig. 5.** Micro-computed tomography (micro-CT) evaluation results. (a) Coronal sections, sagittal reconstructions (right arrows indicate the newly formed bone), and region of interest (ROI) reconstructions (yellow labels highlight the intramedullary nail, white labels indicate the newly formed bone). (b) Quantitative results of bone mineral density (BMD), bone volume (BV), bone volume fraction (BV/TV), trabecular number (Tb.N), trabecular thickness (Tb.Th), and trabecular separation (Tb.Sp) in the ROI. Data represent the mean ± standard deviation ($*p < 0.05$, $**p < 0.01$). (For interpretation of the references to color in this figure legend, the reader is referred to the Web version of this article.)

shows the results 3 weeks after osteomyelitis modeling. The modeling group (MRSA) showed signs of infection; these signs included many inflammatory cell infiltrations and abscess formation, which confirmed the success of osteomyelitis modeling. After the second surgical debridement and implantation of intramedullary nails, the pure Ti group still showed significant signs of infection, whereas the Zn-0.8Li-0.5Ag alloy group showed no signs of infection (Fig. 6b). MRSA-induced osteomyelitis was almost cured completely in the group treated with the Zn-0.8Li-0.5Ag alloy, demonstrating the excellent anti-infection ability of this alloy *in vivo*. The results of Giemsa staining (Fig. 6c and d) were consistent with those of H&E staining. Fig. 6c shows the results 3 weeks after infection modeling. MRSA-induced osteomyelitis had been established, and signs of infection and abscess formation could be observed in the rat femoral medullary cavity. After the implantation of the Zn-0.8Li-0.5Ag alloy intramedullary nail, the signs of osteomyelitis in rats were significantly alleviated, whereas the pure Ti group still showed signs of osteomyelitis (Fig. 6d). These findings confirmed the excellent *in vivo* anti-infection ability of the Zn-0.8Li-0.5Ag alloy.

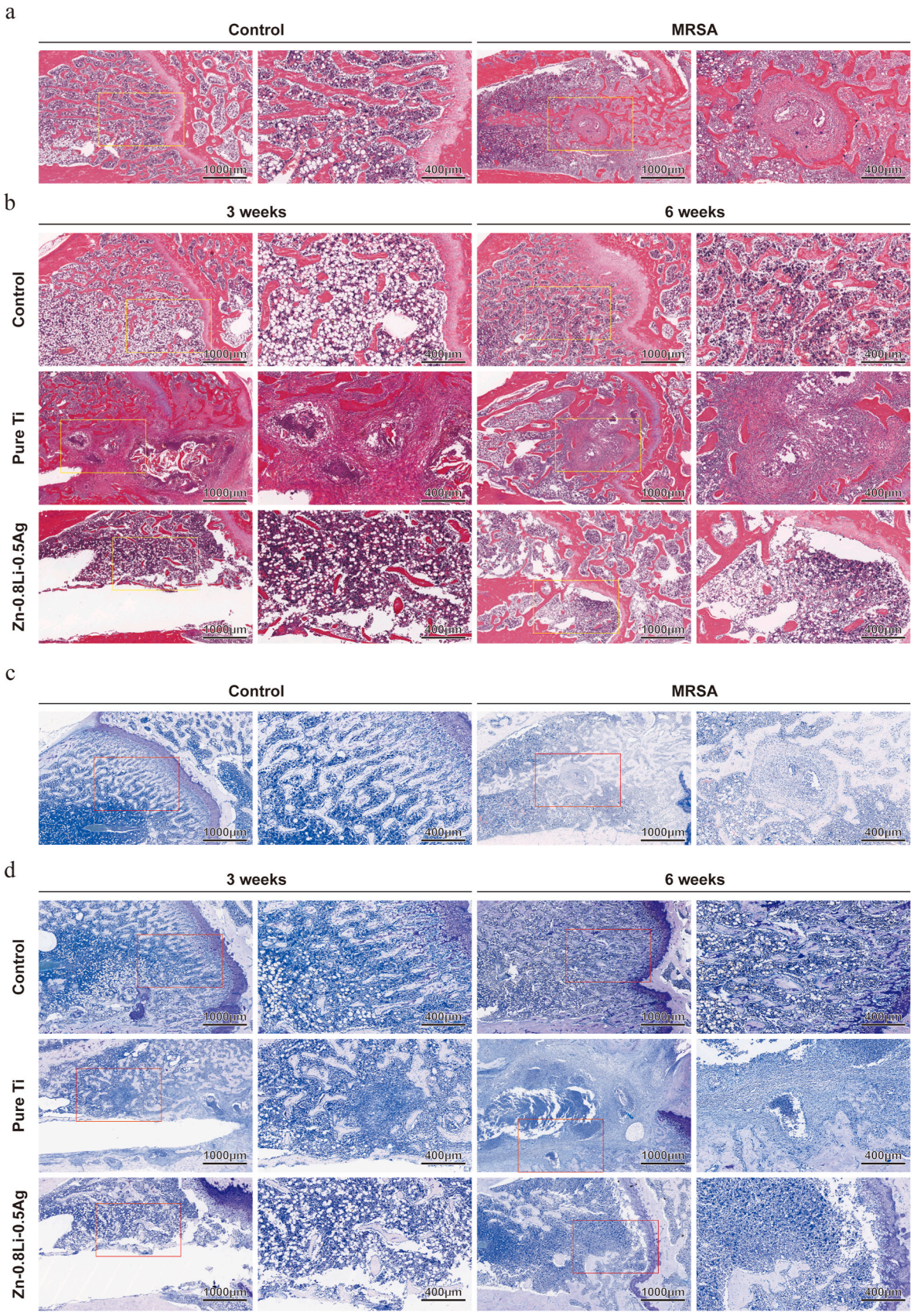


**Fig. 6.** *In vivo* MRSA-induced osteomyelitis treatment results of the Zn-0.8Li-0.5Ag alloy. (a) Hematoxylin and eosin (H&E) staining 3 weeks after osteomyelitis modeling (MRSA indicates osteomyelitis modeling group). (b) H&E staining of rat femurs 3 and 6 weeks after the second surgical debridement and implantation of intramedullary nails (pure Ti or Zn-0.8Li-0.5Ag alloy nails). (c) Giemsa staining 3 weeks after osteomyelitis modeling. (d) Giemsa staining of rat femurs 3 and 6 weeks after the implantation of intramedullary nails.

The results of bone destruction in rats at different time points are shown in Fig. 7. Fig. 7a shows the results of Masson staining; compared with the blank control group, the pure Ti group showed signs of infection and abscess formation with bone destruction 3 and 6 weeks post-operation. Furthermore, disorganized distribution of osteocytes and fibroblast proliferation were observed under high magnification. Moreover, the bone morphology of the Zn-0.8Li-0.5Ag alloy group was almost normal, and no signs of bone destruction were observed. The results of toluidine blue staining confirmed this phenomenon (Fig. 7b). In contrast (Fig. 7c), many abnormally activated mature osteoclasts could be seen in the pure Ti group via TRAP staining. This finding indicated that osteoclasts were activated after the onset of osteomyelitis

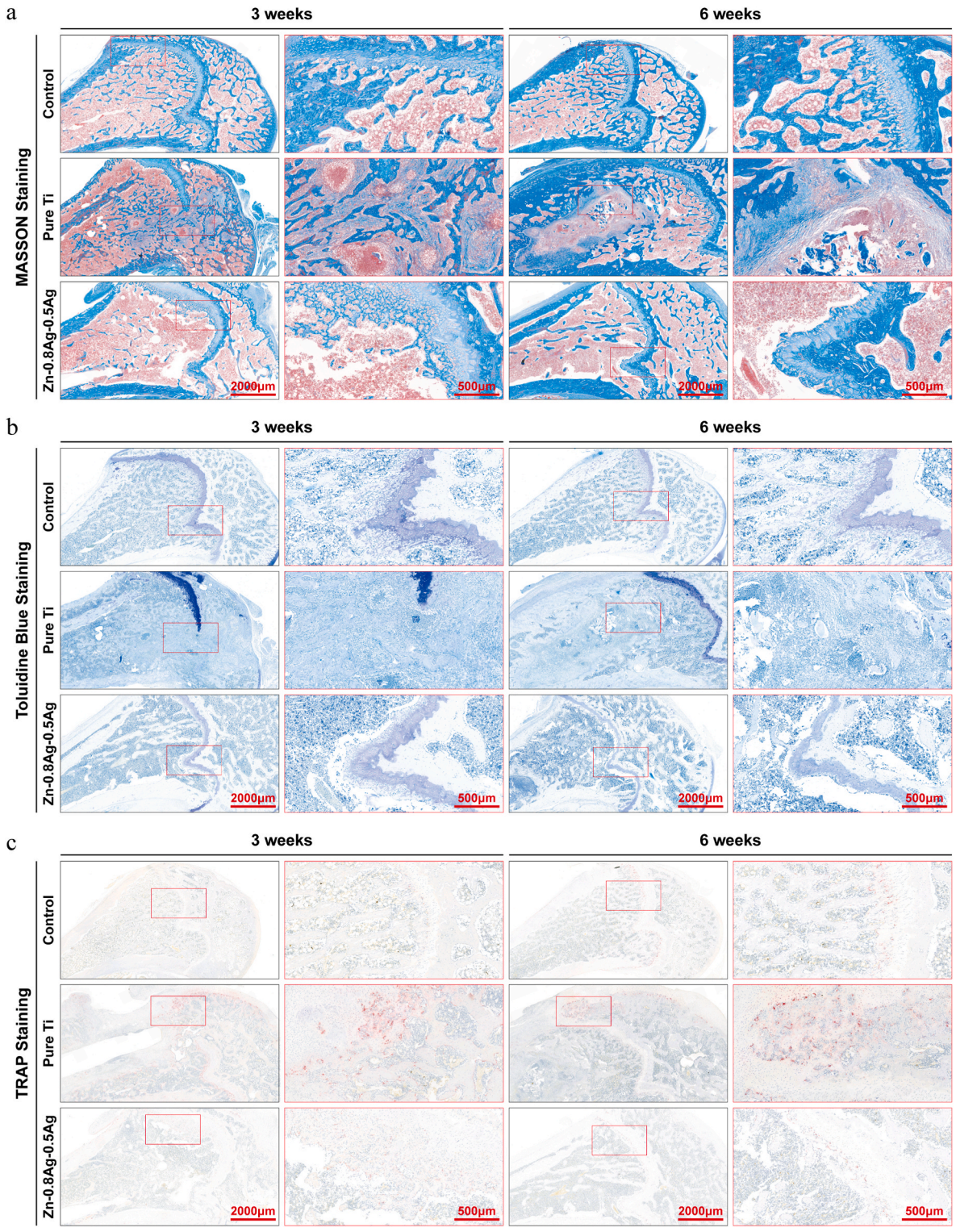


**Fig. 7.** *In vivo* bone destruction prevention of Zn-0.8Li-0.5Ag alloy implants. (a) Masson staining, (b) toluidine blue staining, and (c) TRAP staining of rat femurs 3 and 6 weeks after the implantation of intramedullary nails (pure Ti or Zn-0.8Li-0.5Ag alloy nails). Better bone morphology and significantly less bone destruction were seen in the Zn-0.8Li-0.5Ag alloy group. (For interpretation of the references to color in this figure legend, the reader is referred to the Web version of this article.)

and active bone resorption exacerbated bone destruction, thereby leading to bone loss. In the Zn-0.8Li-0.5Ag alloy group, the activated osteoclasts were comparable to those in the blank control group. These results confirm that Zn-0.8Li-0.5Ag alloy implants can exert osteogenic activity to effectively protect against bone destruction while preventing infection.

#### 3.4.6. Immunohistochemistry results

The immunohistochemical technique was used to evaluate the expression of inflammatory cells (neutrophils, CD68), inflammatory factors (IL-10, TNF-α), and bacteria (MRSA) in rat femur specimens, where brown coloration indicates a positive result. Among the five indices, CD68 is a specific marker for macrophages. The expression of inflammatory cells (neutrophils and macrophages) is shown in Fig. 8a and b. The control and MRSA groups represent the evaluation results of osteomyelitis 3 weeks after modeling. Many inflammatory cells aggregated and wrapped together to form abscesses after infection modeling, indicating the successful establishment of the osteomyelitis model. At 3 and 6 weeks after the implantation of pure Ti and Zn-0.8Li-0.5Ag alloy intramedullary nails, there was no inflammatory cell aggregation in the Zn-0.8Li-0.5Ag alloy group compared with the pure Ti group. This finding indicates that the Zn-0.8Li-0.5Ag alloy group had significantly lower infection than the pure Ti group. This result also suggested the excellent antibacterial ability of the Zn-0.8Li-0.5Ag alloy. The expression levels of inflammatory factors (IL-10 and TNF-α) in each group are shown in Figs. S3 and S4. The significantly higher expression of inflammatory factors in the MRSA group 3 weeks after modeling confirmed the success of osteomyelitis modeling. At 3 and 6 weeks after intramedullary nail implantation, the Zn-0.8Li-0.5Ag group showed significantly lower expression levels of inflammatory factors than the pure Ti group. This result suggests a significantly milder inflammatory response in the Zn-0.8Li-0.5Ag alloy group, confirming the good anti-infection ability of this ternary alloy *in vivo*. Finally, the expression level of MRSA in each group is shown in Fig. S5. Similar to the previous results, the Zn-0.8Li-0.5Ag group showed significantly lower MRSA expression at each time point, which is consistent with the blank control. This result suggests that there were very few residual bacteria in the Zn-0.8Li-0.5Ag alloy group, further confirming the bactericidal ability of this ternary alloy *in vivo*. The corresponding semi-quantitative analysis results are shown in Fig. S6. The semi-quantitative data include positive tissue (%), positive cells (%), and H-score; higher parameters indicate higher expression levels. At different time points, the expression levels of infection indicators were significantly higher in the pure Ti group than in the Zn-0.8Li-0.5Ag alloy group, and those of infection indicators in the Zn-0.8Li-0.5Ag alloy group were comparable to those in the blank control group. This indicates that the infection in the Zn-0.8Li-0.5Ag alloy group almost disappeared, confirming the excellent infection control ability of the Zn-0.8Li-0.5Ag alloy implants.

## 4. Discussion

### 4.1. Antibacterial effects of Zn-Li-Ag alloys

In orthopedic infections, drug-resistant bacteria are an incredibly challenging problem. Among pathogenic bacteria related to infections in orthopedic implants, as many as 40% of *S. epidermidis* [35] and 32% of *S. aureus* [36] isolated from patients are gentamicin-resistant. Multidrug resistance poses an even more complex problem; for instance, MRSA is resistant to not only methicillin but also most β-lactam antibiotics [37]. Generally, β-lactam antibiotics can specifically bind to penicillin-binding proteins (PBPs) and inhibit bacterial cell wall biosynthesis, thereby killing the bacteria [38]. However, in MRSA, PBPs are mutated to PBP2a, which has a significantly lower affinity for β-lactam under the encoding of *mecA* [39]. This activity, thus, greatly reduces the bacteria-killing ability of β-lactam antibiotics [40]. This is believed to be the main mechanism by which MRSA develops resistance to β-lactam antibiotics. In addition to *mecA*-mediated drug resistance, studies have found a series of genes related to *fem* (factors essential for methicillin resistance), *aux* (auxiliary factors), or *hmt* (high methicillin resistance) that contribute to the drug resistance of MRSA [41,42]. Therefore, a variety of alternative antibiotics are becoming less effective because of the growing drug resistance of MRSA. Until now, vancomycin has been considered the last resort for treating clinical infections; however, even vancomycin is sometimes rendered futile when treating MRSA [43]. The multidrug resistance of MRSA makes the treatment of MRSA-related infections extremely difficult. In this situation, traditional antibiotics cannot satisfactorily prevent orthopedic infections.

Compared with antibiotics, metals with bactericidal activities (such as Zn, Ag, and Cu) possess different antimicrobial mechanisms. In this study, the biodegradable Zn-Li-Ag alloys mainly exerted a bactericidal effect through the release of $Zn^{2+}$ and $Ag^{+}$ ions resulting from the degradation of the alloys. Ag exhibits excellent broad-spectrum antibacterial properties and has already been widely used in the clinical domain [44–46]. $Ag^{+}$ can exert bactericidal properties even at a very low concentration of about 0.1 ng/mL to 0.1 μg/mL [47]. Like those of Ag, the broad-spectrum antibacterial properties of Zn have also been widely reported [48–51]. The antibacterial effect of the biodegradable Zn-Li-Ag alloys is mainly achieved through several mechanisms. First, both $Zn^{2+}$ and $Ag^{+}$ can interact with the bacterial surface at the cell membrane level, disrupt the charge balance of the bacterial cell membrane, increase membrane permeability, and lead to bacterial cell rupture and death [23,52]. Second, both ions can exert bactericidal properties by disturbing the basic life activities of bacteria. After $Zn^{2+}$ enters bacteria, it can mismetallate key proteins and enzymes in the metabolic process, inhibit the electron transport chain, and affect the metabolism of bacteria, thereby killing the bacteria [29,53]. After $Ag^{+}$ enters bacteria, it can combine with enzymes and proteins that are essential for bacterial life activities; for example, $Ag^{+}$ can interact with NADH dehydrogenase and inhibit the respiratory electron transport chain [54]. However, $Ag^{+}$ can bind with transporter proteins, leading to proton leakage and, thus, inhibiting proton motive force [55], disturbing bacterial ATP production and DNA replication, and ultimately leading to bacterial cell death. Such an effect is confirmed by the significantly inhibited establishment of localization and transporter activity, as shown in Figs. 2d and 3a. These findings indicate that the Zn-Li-Ag alloy killed bacteria mainly by affecting their basic biological metabolism. Third, both ions can induce the production of ROS ($OH^{-}$, $O_2^{-}$, and $H_2O_2$); $Zn^{2+}$ can exert catalytic activity to induce ROS production in bacteria [56], and $Ag^{+}$ can induce excessive ROS production in bacteria by disturbing the cell respiratory chain [57]. The production of excessive free radicals can cause oxidative stress in cells and damage lipids, DNA, RNA, and proteins, thereby killing bacteria or causing apoptosis [58]. The significantly upregulated catalytic activity and redox reaction shown in Fig. 2d and the higher ROS production of the Zn-0.8Li-0.5Ag group in Fig. 3b confirmed the occurrence of excessive ROS production.

In addition to killing MRSA, the accumulation of $Zn^{2+}$ in the bacterial cytoplasm can mismetallate cytoplasmic proteins, inhibit the biosynthesis of bacterial toxins such as hemolysin, and reduce bacterial virulence [59]. This explains the suppression of genes associated with the bacterial virulence shown in Figs. 2d and 3a. However, $Zn^{2+}$ [60] and $Ag^{+}$ [61] could also inhibit bacterial biofilm formation. Biofilm formation is divided into two steps: colonization of the material surface by bacteria and secretion of extracellular matrix by colonized bacteria to wrap around the bacterium and form a biofilm. The thickening phase of the biofilm is mainly mediated by polysaccharide intercellular adhesin (PIA)-dependent and -independent mechanisms. The main genes encoding PIA are *icaA*, *icaD*, *icaB*, and *icaC*. In Fig. 3a, the expression of icaB and icaC in the Zn-0.8Li-0.5Ag alloy group is significantly suppressed. In addition, as shown in Fig. S2a, there was rare bacterial adherence and no biofilm formation on the surface of Zn-0.8Li-0.5Ag alloy implants; conversely, there was a large amount of bacterial

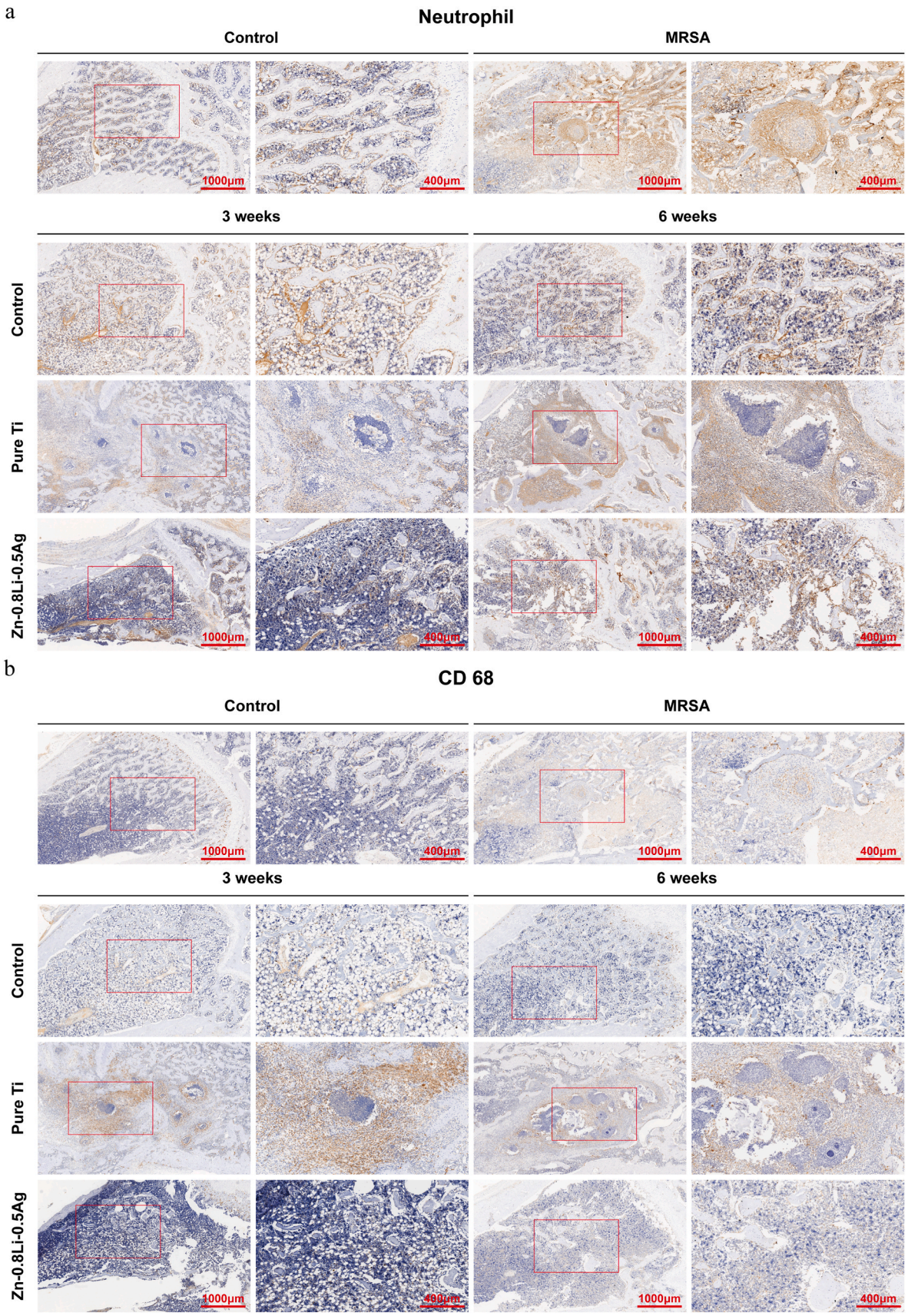


**Fig. 8.** Immunohistochemical evaluation of the treatment effects of the Zn-0.8Li-0.5Ag alloy against methicillin-resistant *Staphylococcus aureus* (MRSA)-induced osteomyelitis. Expression levels of (a) neutrophils and (b) macrophages (CD 68 as the marker). The control group and MRSA group illustrate the establishment of the osteomyelitis model 3 weeks after injecting MRSA suspension. The groups 3 and 6 weeks demonstrated the treatment effects of Zn-0.8Li-0.5Ag alloy or pure Ti nails on osteomyelitis at indicated times after implantation.

adherence and biofilm formation on the surface of pure Ti implants. These results confirmed that the Zn-0.8Li-0.5Ag alloy can also effectively inhibit bacterial biofilm formation and prevent infection. Finally, in terms of drug resistance, previous studies have found that $Zn^{2+}$ can inhibit drug resistance mutations in *Escherichia coli* [62] and reverse the drug resistance in *Streptococcus*, MRSA, and intestinal flora [25]. In this study, as shown in Fig. 3a, the expression of PBP2 in the Zn-0.8Li-0.5Ag group was upregulated, which was conducive to improving the specific binding of β-lactam antibiotics. Furthermore, the expression of *fmhA* (methicillin resistance determinant protein FmhA) was inhibited, indicating that the Zn-0.8Li-0.5Ag alloy alleviates the resistance of MRSA to β-lactam antibiotics. However, the suppressed expression of *tcaB* (teicoplanin resistance-associated membrane protein), *NorA* (quinolone resistance protein), *FosB* (fosfomycin resistance protein), and other genes indicates that the Zn-0.8Li-0.5Ag alloy also alleviates the resistance of MRSA to other antibiotics. This provides a favorable condition for the joint application of the Zn-0.8Li-0.5Ag alloy and antibiotics to prevent osteomyelitis.

### 4.2. Degradation behavior and mechanical properties of Zn-Li-Ag alloys

In addition to its antibacterial properties, the degradation behavior and mechanical properties of the Zn-Li-Ag alloy make it a potential candidate as a biodegradable orthopedic implant material. To be used as a degradable orthopedic implant material, the degradation behavior of zinc alloys is expected to be compatible with the bone repair process. In a preliminary study, we evaluated the *in vivo* degradation behavior of various binary zinc alloys. After installing zinc alloy implants into the femur of mice and keeping the implants for 8 weeks, the *in vivo* degradation rate of zinc alloy has been determined to be about 0.2 mm/year [63]. The slow degradation rate enables the zinc alloy implants to maintain sufficient integrity to provide mechanical support during the early stages of bone repair, effectively avoiding early implant fracture and internal fixation failure owing to too rapid degradation. In addition, the Zn-alloy implant is expected to accelerate the degradation and resorption after the bone repair process is completed. Therefore, we evaluated the degradation behavior of the Zn-Li-Ag alloy for a better degradation rate of the zinc alloy.

As observed from the electrochemical data (Fig. 1e and f), the Zn-Li-Ag alloys were more likely to be degraded than Zn0.8Li. From Table S3, it can be seen that the OCP of Zn-0.8Li was −1.052 V (vs. SCE), and the OCPs of Zn-Li-Ag alloys were very close to each other. The OCP of Zn-0.8Li was higher than that of the Zn-Li-Ag alloys. From the estimated corrosion rates calculated from the $I_{corr}$ data, the corrosion rates of the alloys were observed to be on a similar level, in accordance with the results from the immersion tests. In EIS (Fig. 1f), the shapes of the as-tested alloys were similar. Two distinguished time constants corresponded to two capacitive loops. The capacitive loop at high frequency was associated with the charge transfer process and the electrochemical double layer. The capacitive loop at low frequency was assigned to the corrosion products formed on the surface. The data suggest that the initial degradation rates of Zn-Li-Ag alloys are higher than those of the Zn-0.8Li alloy, which may enhance the degradability of Zn alloys. The degradation rates could also influence the antibacterial performance of the Zn-Li-Ag alloys. The antibacterial effects of these alloys are mainly attributed to $Ag^{+}$; therefore, the bacteriostatic rings of Zn-Li-Ag alloys are larger than those of Zn-0.8Li. However, the amount of released $Ag^{+}$ is not only related to the Ag content of the alloys but also the degradation rate. Fig. 1g shows the degradation rates of these alloys. The degradation rates of Zn-Li-Ag alloys were in the order of Zn-0.8Li-0.5Ag > Zn-0.8Li-1.25Ag > Zn-0.8Li-2.0Ag. The high degradation rate of Zn-0.8Li-0.5Ag may have considerably contributed to its high antibacterial performance.

As shown in Fig. 1c, the Zn-Li-Ag alloys, especially the Zn-0.8Li-0.5Ag alloy, which showed a UTS of 539.89 ± 10.26 MPa and an elongation of 33.5 ± 9.01%, exhibited good mechanical properties. The ductility of alloys improved (Ag wt.% higher than 0.5 wt%) with an increase in Ag amount, in accordance with previous reports on Zn-Ag alloys [34,64]. The comprehensive mechanical properties of biodegradable metals, including Mg and Zn alloys, are shown in Fig. 9. The UTS of the currently available biodegradable Mg alloys is approximately 200–300 MPa, which is significantly lower than that of pure Ti (UTS = 553 ± 1 MPa, Elongation = 26 ± 1%) [65] and, thus, cannot meet the requirements for internal fixation applications in orthopedic load-bearing areas, which strictly limits their clinical applications. Correspondingly, biodegradable Zn alloys possess significantly superior mechanical strength, especially the Zn-Li-Ag alloy evaluated in the present study, the UTS of which is comparable to that of pure Ti, with superior ductility. Therefore, the excellent mechanical strength of the biodegradable Zn-Li-Ag alloy greatly broadens its clinical applications and provides a solid foundation for its broad applications in the future as a novel implant material in orthopedics.

### 4.3. Osteogenic activity and biocompatibility of Zn-Li-Ag alloys

The onset of infection induces a local inflammatory response during which neutrophils show chemotaxis, aggregate, and release a variety of cytokines to activate osteoclasts [93]. *S. aureus* fibronectin-binding proteins (SpA) that are released after *S. aureus* infection can bind to tumor necrosis factor receptor 1 on osteoblast membranes, thereby inducing osteoblast apoptosis and inhibiting osteogenic activity [94]. The activation of osteoclastic behavior and inhibition of osteogenic activity lead to bone destruction and exacerbate the danger of infection. Therefore, for the prevention and treatment of osteomyelitis, it is of great importance that the implant material itself possesses osteogenic activity to effectively prevent bone loss.

Zn plays an important role in bone formation and mineralization [95] by inhibiting osteoclastic bone resorption and promoting osteoblast proliferation and differentiation, thereby playing a biphasic role in increasing bone mass [96–98]. In addition, in a series of previous studies, our group has demonstrated the osteogenic activity of biodegradable Zn alloys both *in vitro* and *in vivo*. We found that a Zn-Sr alloy scaffold effectively promotes bone defects in rat femoral condyles and shows good osseointegration ability [19] and that a Zn-Li alloy implant can be used to fix transverse femoral shaft fractures in rabbits and promoted fracture healing [18]. The Zn-Ag alloy implant exhibited effective antibacterial activity as well as osteoclastic inhibition activity. Moreover, a Zn-Li-Ca alloy scaffold showed good bone repair ability in a rabbit radial large segment bone defect model [16]. In previous studies, we found that Zn alloys exert osteogenic activity through the activation of the Wnt/β-catenin, PI3K/AKT, and MAPK/Erk signaling pathways [18,19,99]. In the present study, we demonstrated by qPCR and western blotting that the Zn-Li-Ag alloys upregulated key genes and proteins for osteogenic differentiation in MC3T3-E1 cells and activated the Wnt/β-catenin, PI3K/AKT, and MAPK/Erk signaling pathways to exert osteogenic activity (Fig. S7). *In vivo*, significantly more new bone and higher BMD were observed around the Zn-Li-Ag alloy implants according to micro-CT scans (Fig. 5). Moreover, according to Masson and toluidine blue staining (Fig. 7a and b), no significant bone destruction was observed in the femur of the rats in the Zn-Li-Ag alloy group, and the bone tissue morphology was intact. According to TRAP staining (Fig. 7c), Zn-Li-Ag alloy implants could effectively inhibit the abnormal osteoclast activation caused by infection and significantly improve bone destruction. The antibacterial activity of the Zn-Li-Ag alloy led to the killing and disappearance of residual bacteria in bone tissue, thereby reducing the inflammatory response and osteoclast activation; in addition, Zn-Li-Ag alloy implants could directly inhibit the differentiation and function of osteoclasts and prevent bone destruction.

Finally, Zn-Li-Ag alloys showed satisfactory cytocompatibility *in vitro* (Fig. S8). The pathological sections of important organs *in vivo*, ion concentrations, and blood biochemical results (Fig. S9) also confirmed its good biosafety *in vivo*.

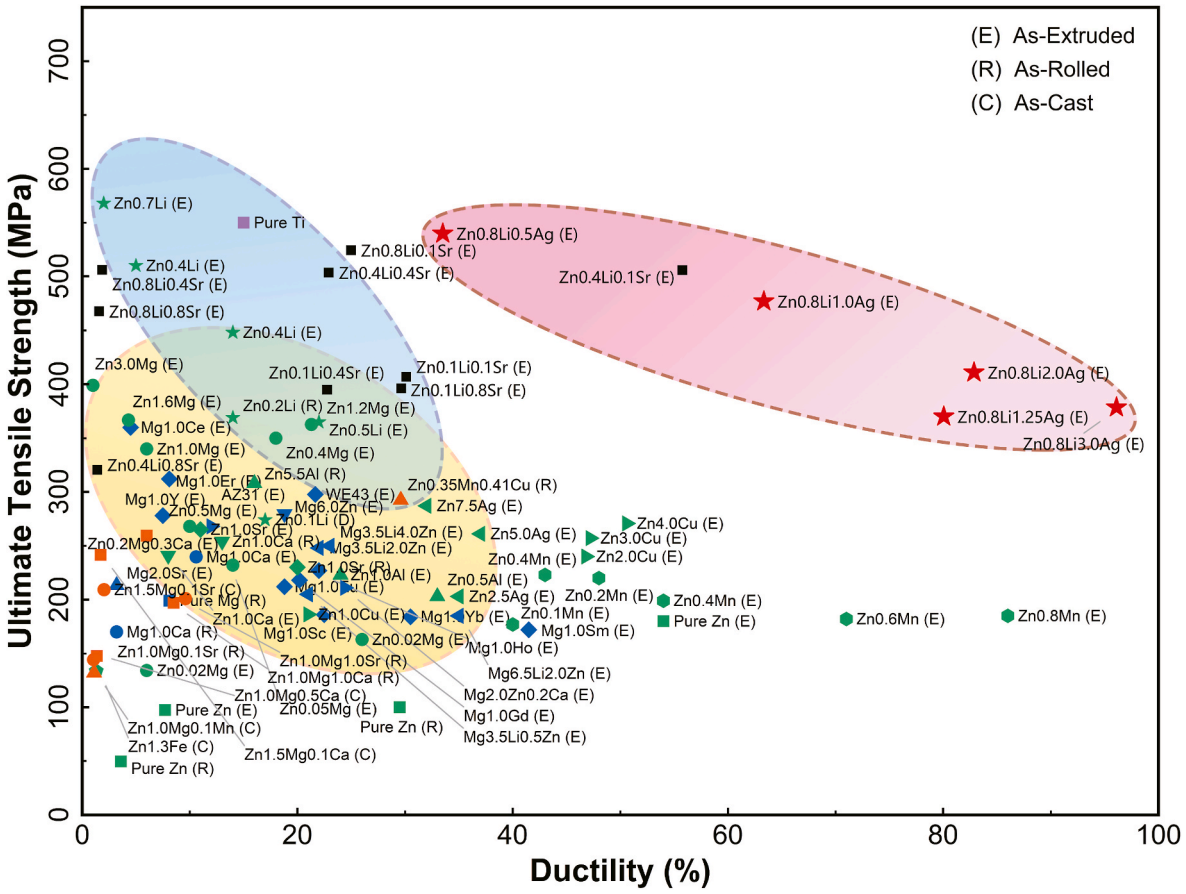


**Fig. 9.** Comprehensive mechanical properties of biodegradable metals, including Mg alloys [66–74], Zn alloys [34,73,75–92], and Zn-Li-Ag alloys discussed in this study.

## 5. Conclusions

The addition of Li and Ag significantly improved the mechanical properties of Zn-Li-Ag alloys, of which Zn-0.8Li-0.5Ag exhibited the best mechanical performance (UTS = 539.89 ± 10.26 MPa; Elong = 33.50 ± 9.01%). The addition of Ag also enhanced the antibacterial activity of Zn-Li-Ag alloys. From the RNA sequencing results, it was found that the Zn-0.8Li-0.5Ag alloy killed MRSA mainly through disturbing cellular metabolism and inducing ROS production; it could also inhibit the biofilm formation and virulence of MRSA and alleviate drug resistance. In addition, Zn-Li-Ag alloys exerted osteogenic activity by activating osteogenic-related signaling pathways and upregulating key osteogenic genes and proteins. The good *in vivo* treatment effect of the Zn-0.8Li-0.5Ag alloy for osteomyelitis was verified in a rat femoral model of MRSA-induced osteomyelitis. The Zn-0.8Li-0.5Ag alloy implants exerted osteogenic activity and significantly improved bone destruction in the treatment of osteomyelitis. Moreover, the results of the blood biochemical tests, ion concentrations in important organs, and pathological sections confirmed that the Zn-0.8Li-0.5Ag alloy is biologically safe *in vivo*.

Taken together, the biodegradable Zn-0.8Li-0.5Ag alloy showed good mechanical strength, ideal biocompatibility, and osteogenic activity, and can effectively kill orthopedic drug-resistant bacteria to prevent and control infections. Owing to these characteristics, we suggest that the Zn-0.8Li-0.5Ag alloy can be an ideal implant material for the preparation of a variety of orthopedic implants, such as steel plates, screws, and intramedullary nails, which are widely used for preventing and treating implant-related infections in orthopedics.

## Credit author statement

**Bo Jia:** Conceptualization, Methodology, Investigation, Writing-original draft, Data curation. **ZeChuan Zhang:** Methodology, Investigation, Writing-review & editing, Data curation. **Yifu Zhuang:** Methodology, Investigation, Writing-review & editing, Data curation. **Hongtao Yang:** Conceptualization, Writing-review & editing, Data curation. **Yu Han:** Methodology, Investigation, Data curation. **Qiang Wu:** Investigation, Investigation. **Xiufeng Jia:** Writing-review & editing. **Yanhui Yin:** Data curation. **Xinhua Qu:** Conceptualization, Writing-review & editing. **Yufeng Zheng:** Conceptualization, Methodology, Resources, Supervision, Writing-review & editing, Project administration, Funding acquisition. **Kerong Dai:** Conceptualization, Methodology, Resources, Supervision, Project administration, Funding acquisition.

## Funding

This work was supported by the National Natural Science Foundation of China [grant numbers 82102540, 51931001].

## Declaration of competing interest

The authors declare that they have no known competing financial interests or personal relationships that could have appeared to influence the work reported in this paper.

## Data availability

Data will be made available on request.

## Appendix A. Supplementary data

Supplementary data to this article can be found online at https://doi.org/10.1016/j.biomaterials.2022.121663.

## References


[1] D.P. Lew, F.A. Waldvogel, Osteomyelitis, Lancet (London, England) 364 (9431) (2004) 369–379.
[2] N. Kavanagh, E.J. Ryan, A. Widaa, G. Sexton, J. Fennell, S. O'Rourke, K.C. Cahill, C.J. Kearney, F.J. O'Brien, S.W. Kerrigan, Staphylococcal osteomyelitis: Disease progression, treatment challenges, and future directions, Clin. Microbiol. Rev. 31 (2) (2018) e00084-17.
[3] K. Merritt, Factors increasing the risk of infection in patients with open fractures, J. Trauma Acute Care Surg. 28 (6) (1988) 823–827.
[4] R. Malhotra, C.S.-Y. Chan, A. Nather, Osteomyelitis in the diabetic foot, Diabet. Foot Ankle 5 (1) (2014), 24445.
[5] D.A. Nardone, Probing to bone in infected pedal ulcers, JAMA 274 (9) (1995) 721–723.
[6] M.V. Belthur, S.B. Birchansky, A.A. Verdugo, E.O.J. Mason, K.G. Hulten, S. L. Kaplan, E. O'Brian Smith, W.A. Phillips, J. Weinberg, Pathologic fractures in children with acute Staphylococcus aureus osteomyelitis, JBJS 94 (1) (2012) 34–42.
[7] W. Costerton, R. Veeh, M. Shirtliff, M. Pasmore, C. Post, G. Ehrlich, The application of biofilm science to the study and control of chronic bacterial infections, J. Clin. Invest. 112 (10) (2003) 1466–1477.
[8] A. Álvarez, L. Fernández, D. Gutiérrez, B. Iglesias, A. Rodríguez, P. García, Methicillin-resistant Staphylococcus aureus in hospitals: latest Trends and treatments based on bacteriophages, J. Clin. Microbiol. 57 (12) (2019) e01006–e01019.
[9] P.N. Reddy, K. Srirama, V.R. Dirisala, An update on clinical burden, diagnostic tools, and therapeutic options of Staphylococcus aureus, Infect. Dis. Res. Treat. 10 (2017), 1179916117703999.
[10] S.I. Berríos-Torres, S.H. Yi, D.W. Bratzler, A. Ma, Y. Mu, L. Zhu, J.A. Jernigan, Activity of commonly used antimicrobial prophylaxis regimens against pathogens causing coronary artery bypass graft and arthroplasty surgical site infections in the United States, 2006-2009, Infect. Control Hosp. Epidemiol. 35 (3) (2014) 231–239.
[11] M.C. Weiser, C.S. Moucha, The current state of screening and decolonization for the prevention of Staphylococcus aureus surgical site infection after total hip and knee arthroplasty, J. Bone Joint Surg. Am. 97 (17) (2015) 1449–1458.
[12] L. Montanaro, P. Speziale, D. Campoccia, S. Ravaioli, I. Cangini, G. Pietrocola, S. Giannini, C.R. Arciola, Scenery of Staphylococcus implant infections in orthopedics, Future Microbiol. 6 (11) (2011) 1329–1349.
[13] H. Lin, Y. Tang, T.P. Lozito, N. Oyster, B. Wang, R.S. Tuan, Efficient in vivo bone formation by BMP-2 engineered human mesenchymal stem cells encapsulated in a projection stereolithographically fabricated hydrogel scaffold, Stem Cell Res. Ther. 10 (1) (2019) 254.
[14] J.M. Schierholz, J. Beuth, Implant infections: a haven for opportunistic bacteria, J. Hosp. Infect. 49 (2) (2001) 87–93.
[15] R.T. Southwood, J.L. Rice, P.J. McDonald, P.H. Hakendorf, M.A. Rozenbilds, Infection in experimental hip arthroplasties, J. Bone Joint Surg. Br. 67 (2) (1985) 229–231.
[16] Z. Zhang, B. Jia, H. Yang, Y. Han, Q. Wu, K. Dai, Y. Zheng, Biodegradable ZnLiCa ternary alloys for critical-sized bone defect regeneration at load-bearing sites: in vitro and in vivo studies, Bioact. Mater. 6 (11) (2021) 3999–4013.
[17] X. Qu, H. Yang, B. Jia, Z. Yu, Y. Zheng, K. Dai, Biodegradable Zn-Cu alloys show antibacterial activity against MRSA bone infection by inhibiting pathogen adhesion and biofilm formation, Acta Biomater. 117 (2020) 400–417.
[18] H. Yang, X. Qu, M. Wang, H. Cheng, B. Jia, J. Nie, K. Dai, Y. Zheng, Zn-0.4Li alloy shows great potential for the fixation and healing of bone fractures at load-bearing sites, Chem. Eng. J. 417 (2021), 129317.
[19] B. Jia, H. Yang, Z. Zhang, X. Qu, X. Jia, Q. Wu, Y. Han, Y. Zheng, K. Dai, Biodegradable Zn–Sr alloy for bone regeneration in rat femoral condyle defect model: in vitro and in vivo studies, Bioact. Mater. 6 (6) (2021) 1588–1604.
[20] H. Yang, B. Jia, Z. Zhang, X. Qu, G. Li, W. Lin, D. Zhu, K. Dai, Y. Zheng, Alloying design of biodegradable zinc as promising bone implants for load-bearing applications, Nat. Commun. 11 (1) (2020) 401.
[21] H. Yang, X. Qu, W. Lin, C. Wang, D. Zhu, K. Dai, Y. Zheng, In vitro and in vivo studies on zinc-hydroxyapatite composites as novel biodegradable metal matrix composite for orthopedic applications, Acta Biomater. 71 (2018) 200–214.
[22] B. Jia, H. Yang, Y. Han, Z. Zhang, X. Qu, Y. Zhuang, Q. Wu, Y. Zheng, K. Dai, In vitro and in vivo studies of Zn-Mn biodegradable metals designed for orthopedic applications, Acta Biomater. 108 (2020) 358–372.
[23] Y.-W. Wang, A. Cao, Y. Jiang, X. Zhang, J.-H. Liu, Y. Liu, H. Wang, Superior antibacterial activity of zinc oxide/graphene oxide composites originating from high zinc concentration localized around bacteria, ACS Appl. Mater. Interfaces 6 (4) (2014) 2791–2798.
[24] H. Umar, D. Kavaz, N. Rizaner, Biosynthesis of zinc oxide nanoparticles using Albizia lebbeck stem bark, and evaluation of its antimicrobial, antioxidant, and cytotoxic activities on human breast cancer cell lines, Int. J. Nanomed. 14 (2019) 87–100.
[25] L. Bohlmann, D.M.P. De Oliveira, I.M. El-Deeb, E.B. Brazel, N. Harbison-Price, C. Y. Ong, T. Rivera-Hernandez, S.A. Ferguson, A.J. Cork, M.D. Phan, A.T. Soderholm, M.R. Davies, G.R. Nimmo, G. Dougan, M.A. Schembri, G.M. Cook, A.G. McEwan, M. von Itzstein, C.A. McDevitt, M.J. Walker, Chemical synergy between ionophore PBT2 and zinc reverses antibiotic resistance, mBio 9 (6) (2018).
[26] X. Qu, H. Yang, B. Jia, M. Wang, B. Yue, Y. Zheng, K. Dai, Zinc alloy-based bone internal fixation screw with antibacterial and anti-osteolytic properties, Bioact. Mater. 6 (12) (2021) 4607–4624.
[27] Z. Li, Z.Z. Shi, Y. Hao, H.F. Li, X.F. Liu, A.A. Volinsky, H.J. Zhang, L.N. Wang, High-performance hot-warm rolled Zn-0.8Li alloy with nano-sized metastable precipitates and sub-micron grains for biodegradable stents, J. Mater. Sci. Technol. 35 (11) (2019) 2618–2624.
[28] Y. Zhuang, L. Ren, S. Zhang, X. Wei, K. Yang, K. Dai, Antibacterial effect of a copper-containing titanium alloy against implant-associated infection induced by methicillin-resistant Staphylococcus aureus, Acta Biomater. 119 (2021) 472–484.
[29] J.R. Sheldon, E.P. Skaar, Metals as phagocyte antimicrobial effectors, Curr. Opin. Immunol. 60 (2019) 1–9.
[30] M.A. Quinteros, V. Cano Aristizábal, P.R. Dalmasso, M.G. Paraje, P.L. Páez, Oxidative stress generation of silver nanoparticles in three bacterial genera and its relationship with the antimicrobial activity, Toxicol. Vitro 36 (2016) 216–223.
[31] M.S. Smeltzer, J.R. Thomas, S.G. Hickraon, R.A. Skinner, C.L. Nelson, D. Griffith, T. R. Parr, R.P. Evans, Characterization of a rabbit model of staphylococcal osteomyelitis, J. Orthop. Res. 15 (3) (1997) 414–421.
[32] Y. Li, L. Liu, P. Wan, Z. Zhai, Z. Mao, Z. Ouyang, D. Yu, Q. Sun, L. Tan, L. Ren, Z. Zhu, Y. Hao, X. Qu, K. Yang, K. Dai, Biodegradable Mg-Cu alloy implants with antibacterial activity for the treatment of osteomyelitis: in vitro and in vivo evaluations, Biomaterials 106 (2016) 250–263.
[33] Kristin Persson, Materials Data on LiZn3 (SG:194) by Materials Project, 2016. https://materialsproject.org/materials/mp-975799/.
[34] M. Sikora-Jasinska, E. Mostaed, A. Mostaed, R. Beanland, D. Mantovani, M. Vedani, Fabrication, mechanical properties and in vitro degradation behavior of newly developed ZnAg alloys for degradable implant applications, Mater. Sci. Eng. C Mater. Biol. Appl. 77 (2017) 1170–1181.
[35] D. Campoccia, L. Montanaro, C.V. Eiff, V. Pirini, S. Ravaioli, K. Becker, C. R. Arciola, Cluster analysis of ribotyping profiles of *Staphylococcus epidermidis* isolates recovered from foreign body-associated orthopedic infections, J. Biomed. Mater. Res. A 88A (3) (2008) 664–672.
[36] D. Campoccia, L. Baldassarri, V. Pirini, S. Ravaioli, L. Montanaro, C.R. Arciola, Molecular epidemiology of Staphylococcus aureus from implant orthopaedic infections: ribotypes, agr polymorphism, leukocidal toxins and antibiotic resistance, Biomaterials 29 (30) (2008) 4108–4116.
[37] K.A. Rodvold, K.W. McConeghy, Methicillin-resistant Staphylococcus aureus therapy: past, present, and future, Clin. Infect. Dis. 58 (Suppl 1) (2014) S20–S27.
[38] S.J. Peacock, G.K. Paterson, Mechanisms of methicillin resistance in Staphylococcus aureus, Annu. Rev. Biochem. 84 (2015) 577–601.
[39] K. Ubukata, R. Nonoguchi, M. Matsuhashi, M. Konno, Expression and inducibility in Staphylococcus aureus of the mecA gene, which encodes a methicillin-resistant S. aureus-specific penicillin-binding protein, J. Bacteriol. 171 (5) (1989) 2882–2885.
[40] B.J. Hartman, Low-affinity penicillin-binding protein associated with β-lactam resistance in Staphylococcus aureus, J. Bacteriol. 158 (2) (1984) 513–516.
[41] B. Berger-Bachi, A. Strassle, J.E. Gustafson, F.H. Kayser, Mapping and characterization of multiple chromosomal factors involved in methicillin resistance in Staphylococcus aureus, Antimicrob. Agents Chemother. 36 (7) (1992) 1367–1373.
[42] H.D. Lencastre, S.W. Wu, M.G. Pinho, A.M. Ludovice, A. Tomasz, Antibiotic resistance as a stress response: complete sequencing of a large number of chromosomal loci in Staphylococcus aureus strain COL that impact on the expression of resistance to methicillin, Microb. Drug Resist. 5 (3) (1999) 163–175.
[43] V.N. Kos, C.A. Desjardins, A. Griggs, G. Cerqueira, T.A. Van, M.T. Holden, P. Godfrey, K.L. Palmer, K. Bodi, E.F. Mongodin, Comparative genomics of vancomycin-resistant Staphylococcus aureus strains and their positions within the clade most commonly associated with Methicillin-resistant S. aureus hospital-acquired infection in the United States, mBio 3 (3) (2012) e00112-12.
[44] J.W. Alexander, History of the medical use of silver, Surg. Infect. (Larchmt) 10 (3) (2009) 289–292.
[45] W. Ngeontae, W. Janrungroatsakul, P. Maneewattanapinyo, S. Ekgasit, W. Aeungmaitrepirom, T. Tuntulani, Novel potentiometric approach in glucose biosensor using silver nanoparticles as redox marker, Sens. Actuators, B 137 (1) (2009) 320–326.
[46] P.C. Lee, D. Meisel, Adsorption and surface-enhanced Raman of dyes on silver and gold sols, J. Phys. Chem. 86 (17) (1982) 3391–3395.
[47] J.Y. Maillard, P. Hartemann, Silver as an antimicrobial: facts and gaps in knowledge, Crit. Rev. Microbiol. 39 (4) (2013) 373–383.
[48] M.F. Khan, A.H. Ansari, M. Hameedullah, E. Ahmad, F.M. Husain, Q. Zia, U. Baig, M.R. Zaheer, M.M. Alam, A.M. Khan, Z.A. AlOthman, I. Ahmad, G.M. Ashraf, G. Aliev, Sol-gel synthesis of thorn-like ZnO nanoparticles endorsing mechanical stirring effect and their antimicrobial activities: potential role as nano-antibiotics, Sci. Rep. 6 (2016), 27689.
[49] H. Chen, M. Zhang, B. Li, D. Chen, X. Dong, Y. Wang, Y. Gu, Versatile antimicrobial peptide-based ZnO quantum dots for in vivo bacteria diagnosis and treatment with high specificity, Biomaterials 53 (2015) 532–544.
[50] Y.H. Zou, J. Wang, L.Y. Cui, R.C. Zeng, Q.Z. Wang, Q.X. Han, J. Qiu, X.B. Chen, D. C. Chen, S.K. Guan, Y.F. Zheng, Corrosion resistance and antibacterial activity of zinc-loaded montmorillonite coatings on biodegradable magnesium alloy AZ31, Acta Biomater. 98 (2019) 196–214.
[51] R. Nunes, P. Pasko, M. Tyszka-Czochara, A. Szewczyk, M. Szlosarczyk, I. S. Carvalho, Antibacterial, antioxidant and anti-proliferative properties and zinc content of five south Portugal herbs, Pharm. Biol. 55 (1) (2017) 114–123.

[52] S. Silver, T. Phung le, G. Silver, Silver as biocides in burn and wound dressings and bacterial resistance to silver compounds, J. Ind. Microbiol. Biotechnol. 33 (7) (2006) 627–634.
[53] K.S. Siddiqi, A. Ur Rahman, Tajuddin, A. Husen, Properties of zinc oxide nanoparticles and their activity against microbes, Nanoscale Res. Lett. 13 (1) (2018) 141.
[54] C. Marambio-Jones, E.M.V. Hoek, A review of the antibacterial effects of silver nanomaterials and potential implications for human health and the environment, J. Nanoparticle Res. 12 (5) (2010) 1531–1551.
[55] C.-N. Lok, C.-M. Ho, R. Chen, Q.-Y. He, W.-Y. Yu, H. Sun, P.K.-H. Tam, J.-F. Chiu, C.-M. Che, Proteomic analysis of the mode of antibacterial action of silver nanoparticles, J. Proteome Res. 5 (4) (2006) 916–924.
[56] S. Kargozar, M. Montazerian, S. Hamzehlou, H.W. Kim, F. Baino, Mesoporous bioactive glasses: promising platforms for antibacterial strategies, Acta Biomater. 81 (2018) 1–19.
[57] H.-J. Park, J.Y. Kim, J. Kim, J.-H. Lee, J.-S. Hahn, M.B. Gu, J. Yoon, Silver-ion-mediated reactive oxygen species generation affecting bactericidal activity, Water Res. 43 (4) (2009) 1027–1032.
[58] T. Xia, M. Kovochich, J. Brant, M. Hotze, J. Sempf, T. Oberley, C. Sioutas, J.I. Yeh, M.R. Wiesner, A.E. Nel, Comparison of the abilities of ambient and manufactured nanoparticles to induce cellular toxicity according to an oxidative stress paradigm, Nano Lett. 6 (8) (2006) 1794–1807.
[59] P. Chandrangsu, J.D. Helmann, Intracellular Zn(II) intoxication leads to dysregulation of the PerR regulon resulting in heme toxicity in Bacillus subtilis, PLoS Genet. 12 (12) (2016), e1006515.
[60] J.H. Lim, Y. Jeong, S.H. Song, J.H. Ahn, J.R. Lee, S.M. Lee, Penetration of an antimicrobial zinc-sugar alcohol complex into Streptococcus mutans biofilms, Sci. Rep. 8 (1) (2018), 16154.
[61] V. Kostenko, J. Lyczak, K. Turner, R.J. Martinuzzi, Impact of silver-containing wound dressings on bacterial biofilm viability and susceptibility to antibiotics during prolonged treatment, Antimicrob. Agents Chemother. 54 (12) (2010) 5120–5131.
[62] J.K. Crane, M.B. Cheema, M.A. Olyer, M.D. Sutton, Zinc blockade of SOS response inhibits horizontal transfer of antibiotic resistance genes in enteric bacteria, Front. Cell. Infect. Microbiol. 8 (2018) 410.
[63] H.F. Li, X.H. Xie, Y.F. Zheng, Y. Cong, F.Y. Zhou, K.J. Qiu, X. Wang, S.H. Chen, L. Huang, L. Tian, L. Qin, Development of biodegradable Zn-1X binary alloys with nutrient alloying elements Mg, Ca and Sr, Sci. Rep. 5 (2015), 10719.
[64] P. Li, C. Schille, E. Schweizer, F. Rupp, A. Heiss, C. Legner, U.E. Klotz, J. Geis-Gerstorfer, L. Scheideler, Mechanical characteristics, in vitro degradation, cytotoxicity, and antibacterial evaluation of Zn-4.0Ag alloy as a biodegradable material, Int. J. Mol. Sci. 19 (3) (2018) 755.
[65] Y. Okazaki, A. Ishino, Microstructures and mechanical properties of laser-sintered commercially pure Ti and Ti-6Al-4V alloy for dental applications, Materials (Basel) 13 (3) (2020) 609.
[66] Z. Li, X. Gu, S. Lou, Y. Zheng, The development of binary Mg-Ca alloys for use as biodegradable materials within bone, Biomaterials 29 (10) (2008) 1329–1344.
[67] Y.F. Zheng, X.N. Gu, F. Witte, Biodegradable metals, Mater. Sci. Eng. R 77 (2014) 1–34.
[68] Y. Liu, Y. Wu, D. Bian, S. Gao, S. Leeflang, H. Guo, Y. Zheng, J. Zhou, Study on the Mg-Li-Zn ternary alloy system with improved mechanical properties, good degradation performance and different responses to cells, Acta Biomater. 62 (2017) 418–433.
[69] X.N. Gu, X.H. Xie, N. Li, Y.F. Zheng, L. Qin, In vitro and in vivo studies on a Mg-Sr binary alloy system developed as a new kind of biodegradable metal, Acta Biomater. 8 (6) (2012) 2360–2374.
[70] D. Bian, W. Zhou, J. Deng, Y. Liu, W. Li, X. Chu, P. Xiu, H. Cai, Y. Kou, B. Jiang, Y. Zheng, Development of magnesium-based biodegradable metals with dietary trace element germanium as orthopaedic implant applications, Acta Biomater. 64 (2017) 421–436.
[71] M.I. Sabir, X. Xu, L. Li, A review on biodegradable polymeric materials for bone tissue engineering applications, J. Mater. Sci. 44 (21) (2009) 5713–5724.
[72] J. Liu, D. Bian, Y. Zheng, X. Chu, Y. Lin, M. Wang, Z. Lin, M. Li, Y. Zhang, S. Guan, Comparative in vitro study on binary Mg-RE (Sc, Y, La, Ce, Pr, Nd, Sm, Eu, Gd, Tb, Dy, Ho, Er, Tm, Yb and Lu) alloy systems, Acta Biomater. 102 (2020) 508–528.
[73] H. Hermawan, D. Dube, D. Mantovani, Developments in metallic biodegradable stents, Acta Biomater. 6 (5) (2010) 1693–1697.
[74] P. Han, P. Cheng, S. Zhang, C. Zhao, J. Ni, Y. Zhang, W. Zhong, P. Hou, X. Zhang, Y. Zheng, Y. Chai, In vitro and in vivo studies on the degradation of high-purity Mg (99.99wt.%) screw with femoral intracondylar fractured rabbit model, Biomaterials 64 (2015) 57–69.
[75] E. Mostaed, M. Sikora-Jasinska, A. Mostaed, S. Loffredo, A.G. Demir, B. Previtali, D. Mantovani, R. Beanland, M. Vedani, Novel Zn-based alloys for biodegradable stent applications: design, development and in vitro degradation, J. Mech. Behav. Biomed. Mater. 60 (2016) 581–602.
[76] E. Mostaed, M. Sikora-Jasinska, J.W. Drelich, M. Vedani, Zinc-based alloys for degradable vascular stent applications, Acta Biomater. 71 (15) (2018) 1–23.
[77] Y. Liu, Y. Zheng, X.-H. Chen, J.-A. Yang, H. Pan, D. Chen, L. Wang, J. Zhang, D. Zhu, S. Wu, K.W.K. Yeung, R.-C. Zeng, Y. Han, S. Guan, Fundamental theory of biodegradable metals-definition, criteria, and design, Adv. Funct. Mater. 29 (18) (2019), 1805402.
[78] X. Liu, J. Sun, F. Zhou, Y. Yang, R. Chang, K. Qiu, Z. Pu, L. Li, Y. Zheng, Micro-alloying with Mn in Zn–Mg alloy for future biodegradable metals application, Mater. Des. 94 (2016) 95–104.
[79] H.F. Li, X.H. Xie, Y.F. Zheng, Y. Cong, F.Y. Zhou, K.J. Qiu, X. Wang, S.H. Chen, L. Huang, L. Tian, L. Qin, Development of biodegradable Zn-1X binary alloys with nutrient alloying elements Mg, Ca and Sr, Sci. Rep. 5 (2015), 10719.
[80] B. Jia, H. Yang, Y. Han, Z. Zhang, X. Qu, Y. Zhuang, Q. Wu, Y. Zheng, K. Dai, In vitro and in vivo studies of Zn-Mn biodegradable metals designed for orthopedic applications, Acta Biomater. 108 (2020) 358–372.
[81] Y.X. Yin, C. Zhou, Y.P. Shi, Z.Z. Shi, T.H. Lu, Y. Hao, C.H. Liu, X. Wang, H.J. Zhang, L.N. Wang, Hemocompatibility of biodegradable Zn-0.8wt% (Cu, Mn, Li) alloys, Mater. Sci. Eng. C Mater. Biol. Appl. 104 (2019), 109896.
[82] G. Li, H. Yang, Y. Zheng, X.H. Chen, J.A. Yang, D. Zhu, L. Ruan, K. Takashima, Challenges in the use of zinc and its alloys as biodegradable metals: perspective from biomechanical compatibility, Acta Biomater. 97 (2019) 23–45.
[83] Z. Tang, J. Niu, H. Huang, H. Zhang, J. Pei, J. Ou, G. Yuan, Potential biodegradable Zn-Cu binary alloys developed for cardiovascular implant applications, J. Mech. Behav. Biomed. Mater. 72 (2017) 182–191.
[84] W. Yuan, D. Xia, Y. Zheng, X. Liu, S. Wu, B. Li, Y. Han, Z. Jia, D. Zhu, L. Ruan, K. Takashima, Y. Liu, Y. Zhou, Controllable biodegradation and enhanced osseointegration of ZrO2-nanofilm coated Zn-Li alloy: in vitro and in vivo studies, Acta Biomater. 105 (2020) 290–303.
[85] Z.-Z. Shi, J. Yu, X.-F. Liu, L.-N. Wang, Fabrication and characterization of novel biodegradable Zn-Mn-Cu alloys, J. Mater. Sci. Technol. 34 (6) (2017) 1008–1015.
[86] X. Liu, J. Sun, Y. Yang, F. Zhou, Z. Pu, L. Li, Y. Zheng, Microstructure, mechanical properties, in vitro degradation behavior and hemocompatibility of novel Zn–Mg–Sr alloys as biodegradable metals, Mater. Lett. 162 (2016) 242–245.
[87] F. Zivic, S. Affatato, M. Trajanovic, M. Schnabelrauch, N. Grujovic, K.L. Choy, Biomaterials in Clinical Practice, 2017. Springer.
[88] L.-Q. Wang, Y.-P. Ren, S.-N. Sun, H. Zhao, S. Li, G.-W. Qin, Microstructure, mechanical properties and fracture behavior of as-extruded Zn–Mg binary alloys, Acta Metall. Sin. (Engl. Lett.) 30 (10) (2017) 931–940.
[89] H. Guo, D. Xia, Y. Zheng, Y. Zhu, Y. Liu, Y. Zhou, A pure zinc membrane with degradability and osteogenesis promotion for guided bone regeneration: in vitro and in vivo studies, Acta Biomater. 106 (2020) 396–409.
[90] A. Kafri, S. Ovadia, J. Goldman, J. Drelich, E. Aghion, The suitability of Zn–1.3%Fe alloy as a biodegradable implant material, Metals 8 (3) (2018) 153–167.
[91] H.-S. Han, S. Loffredo, I. Jun, J. Edwards, Y.-C. Kim, H.-K. Seok, F. Witte, D. Mantovani, S. Glyn-Jones, Current status and outlook on the clinical translation of biodegradable metals, Mater. Today 23 (2019) 57–71.
[92] Z. Zhang, B. Jia, H. Yang, Y. Han, Q. Wu, K. Dai, Y. Zheng, Zn0.8Li0.1Sr—a biodegradable metal with high mechanical strength comparable to pure Ti for the treatment of osteoporotic bone fractures: in vitro and in vivo studies, Biomaterials 275 (2021), 120905.
[93] U. Dapunt, T. Giese, S. Maurer, S. Stegmaier, B. Prior, G.M. Hänsch, M.M. Gaida, Neutrophil-derived MRP-14 is up-regulated in infectious osteomyelitis and stimulates osteoclast generation, J. Leukoc. Biol. 98 (4) (2015) 575–582.
[94] A. Widaa, T. Claro, T.J. Foster, F.J. O'Brien, S.W. Kerrigan, Staphylococcus aureus protein A plays a critical role in mediating bone destruction and bone loss in osteomyelitis, PLoS One 7 (7) (2012), e40586.
[95] K.A. McCall, C. Huang, C.A. Fierke, Function and mechanism of zinc metalloenzymes, J. Nutr. 130 (5S Suppl) (2000), 1437s-46s.
[96] M. Yamaguchi, Role of nutritional zinc in the prevention of osteoporosis, Mol. Cell. Biochem. 338 (1–2) (2010) 241–254.
[97] X. Fu, Y. Li, T. Huang, Z. Yu, K. Ma, M. Yang, Q. Liu, H. Pan, H. Wang, J. Wang, M. Guan, Runx2/Osterix and zinc uptake synergize to orchestrate osteogenic differentiation and citrate containing bone apatite formation, Adv. Sci. (Weinh) 5 (4) (2018), 1700755.
[98] H.J. Seo, Y.E. Cho, T. Kim, H.I. Shin, I.S. Kwun, Zinc may increase bone formation through stimulating cell proliferation, alkaline phosphatase activity and collagen synthesis in osteoblastic MC3T3-E1 cells, Nutr. Res. Pract. 4 (5) (2010) 356–361.
[99] D. Zhu, I. Cockerill, Y. Su, Z. Zhang, J. Fu, K.W. Lee, J. Ma, C. Okpokwasili, L. Tang, Y. Zheng, Y.X. Qin, Y. Wang, Mechanical strength, biodegradation, and in vitro and in vivo biocompatibility of Zn biomaterials, ACS Appl. Mater. Interfaces 11 (7) (2019) 6809–6819.